

contrast agents are mainly extracellular agents with nonspecific biodistribution.^[4,5] In contrast, it is also possible to develop Gd^{3+} complexes with various chemical properties by means of appropriate ligand design for Gd^{3+} ,^[6] and, indeed, some bioactivated MRI contrast agents have been reported for monitoring enzyme activity, Ca^{2+} , pH, $p(O_2)$, Zn^{2+} , and so on.^[7] These MRI contrast agents show a change in the water proton relaxation time (T_1 or T_2) in response to the presence of specific biomolecules. Recently, attempts have been made to utilize MR imaging techniques to detect gene expression, and the development of these methods would allow MR imaging of the expression of specific genes.^[8] For example, β -galactosidase is a commonly used gene expression marker, that is, gene expression is monitored by introducing a marker gene, lacZ, to follow the regulation of a gene of interest because it can easily be assayed and is not normally expressed in most mammalian tissues or cells.^[9] Meade and co-workers developed the bioactivated MRI contrast agent, EgadMe, which reports on β -galactosidase activity to image the expression of a transgene.^[10] The mechanism of the T_1 relaxation time change between two distinct relaxation states, long and short, is as follows. The enzyme substrate, galactopyranose, which is linked to the ligand, blocks the one remaining open coordination site of the chelated Gd^{3+} , inhibiting access of water to the chelated Gd^{3+} ion. The contrast agent is switched on when β -galactosidase cleaves the galactopyranose from the Gd^{3+} complex and the chelated Gd^{3+} ion becomes accessible to water. This agent has been successfully used in vivo to monitor gene expression in *Xenopus laevis*.^[10a] Thus, this MRI contrast agent showed a change in the longitudinal relaxation time (T_1) in the presence of β -galactosidase by modulating the access of water molecules to the chelated Gd^{3+} ion. In addition to above results, β -galactosidase-activated MRI contrast agents with a range of chemical properties are also needed for further biological studies, so the development of novel β -galactosidase-activated MRI contrast agents with a different design approach would be helpful for studies of biological phenomena by monitoring gene expression. One possible approach for the development of biomolecule-activated MRI contrast agents is the RIME (receptor-induced magnetization enhancement) approach.^[11] The binding of a MRI contrast agent to a macromolecule substantially slows molecular rotation of the Gd^{3+} complex, resulting in an additional increase in the r_1 relaxivity through the rotational correlation time τ_R .^[2] When the Gd^{3+} complex binds to a macromolecule, the τ_R increases from that of a small molecule to that of the protein, and the r_1 relaxivity increases. The slower the Gd^{3+} complex tumbles, the longer the τ_R , leading to faster relaxation rates and, hence, higher r_1 relaxivity. The τ_R for small Gd^{3+} complexes is usually in the picosecond range (typically 50–200 ps), whereas the τ_R for a macromolecule such as albumin is in the nanosecond range (about 50 ns).^[6a] This phenomenon is known as RIME. RIME agents have been reported for alkaline phosphatase and for carboxypeptidase B (part of the thrombin-activatable fibrinolysis inhibitor family), which regulate noncovalent binding

of the agents to human serum albumin (HSA).^[12,13] Another agent permitted the detection of yeast transcription repressor or protein (Gal80) as MR images by utilizing a specific peptide-protein binding event,^[14] and the enzyme carbonic anhydrase was selectively targeted with a sulfonamide substituent.^[15] Moreover, oligonucleotide sequences have also been detected with iron oxide nanoparticles derivatized with oligonucleotide.^[16] Hybridization with oligonucleotide-derived particles resulted in changes mainly in the spin-spin relaxation time (T_2) of adjacent water protons. Efficient polymerization of Gd^{3+} complexes can also be used to directly image the activity of enzymes such as myeloperoxidase (MPO) and matrix metalloproteinase 2 (MMP-2).^[17,18]

Here, we report the design and synthesis of a novel β -galactosidase-activated MRI contrast agent based on the RIME approach (Figure 1). Reaction with β -galactosidase

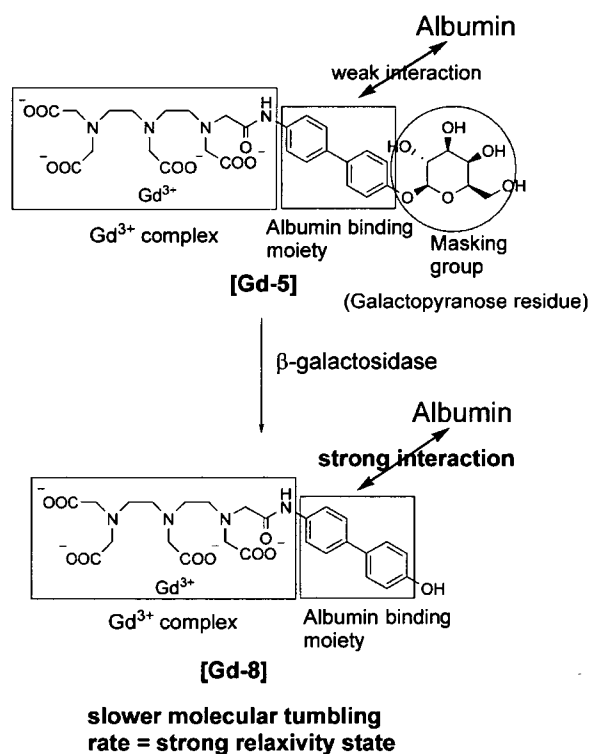


Figure 1. The RIME mechanism for the β -galactosidase-activated MRI contrast agent [Gd-5]. In [Gd-5], a Gd^{3+} complex is coupled to an albumin binding moiety that is masked by the galactopyranose residue. The galactopyranose residue of [Gd-5] is designed to be cleaved by β -galactosidase, transforming [Gd-5] to [Gd-8], and this cleavage promotes albumin binding of the Gd^{3+} complex.

yielded a 57% increase in the r_1 relaxivity in phosphate-buffered saline (PBS) with 4.5% w/v HSA. Cleavage of the galactopyranose moiety from the aryl group of the Gd^{3+} complex increases the hydrophobicity of the aryl group, thereby increasing the HSA binding affinity. The greater binding of the Gd^{3+} complex to the macromolecule, HSA, increases

the r_1 relaxivity. We also confirmed the mechanism of this increase in the r_1 relaxivity.

Results and Discussion

Design and synthesis of [Gd-5] and [Gd-8]: The Gd³⁺ complex, [Gd-5], was designed to detect β -galactosidase activity through conversion of the MRI-silent agent into an activated MRI agent, [Gd-8] (Figure 1). The [Gd-5] is composed of three moieties: 1) a masking group consisting of galactopyranose; 2) an albumin-binding moiety, the biphenyl group; 3) an MRI signal-generating moiety, which is a Gd³⁺ complex. This design relies upon enzymatic transformation of a Gd³⁺ complex with poor albumin affinity and concomitant low relaxivity into one with high albumin affinity and high relaxivity. The biphenyl group was selected as the albumin binding group, because the biphenyl residue is known to possess high albumin binding affinity.^[4,13,19] A substrate for β -galactosidase, galactopyranose, was used as a masking group, affording extremely high hydrophilicity compared with the hydrophobicity of the biphenyl group. Hydrolysis of the galactopyranose moiety unblocks the hydrophobicity of the biphenyl group, thereby increasing the albumin binding affinity. Thus, in [Gd-5], a masking group that inhibits albumin binding was expected to be removed by the enzymatic activity, to expose an albumin-binding group with high affinity. The strong interaction of the Gd³⁺ complex with a macromolecule such as albumin increases the r_1 relaxivity owing to the RIME phenomenon. The synthetic schemes for the lanthanide complexes, [Gd-5] and [Gd-8], and details of the chemical characterization of compounds are provided in the Supporting Information.

Longitudinal relaxation time T_1 measurements of [Gd-5] with β -galactosidase: The longitudinal relaxation times T_1 of [Gd-5] were measured in the presence of β -galactosidase or heat-inactivated β -galactosidase with 4.5% w/v HSA in phosphate-buffered saline (PBS; pH 7.4), at 20 MHz (0.47 T), at 37 °C (Figure 2). The value of $1/T_1$ increased

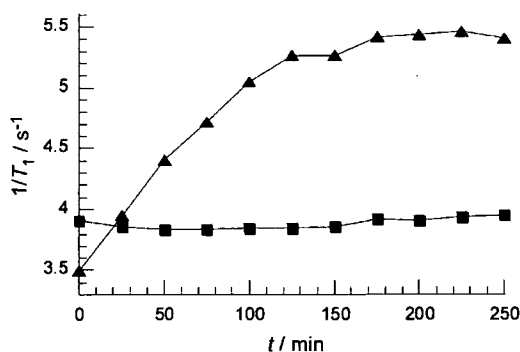


Figure 2. Time course of the β -galactosidase-induced (113 nM; \blacktriangle) and heat-inactivated β -galactosidase-induced (113 nM; \blacksquare) changes in the value of $1/T_1$ [s^{-1}], of 0.5 mM [Gd-5] solution at 20 MHz, 37 °C in phosphate-buffered saline (PBS; pH 7.4) with 4.5% w/v human serum albumin (HSA).

from 3.5 to 5.5 s⁻¹ between 0 and 250 min in the presence of β -galactosidase (113 nM), whereas the value of $1/T_1$ changed only slightly from 3.8 to 4.0 s⁻¹ between 0 and 250 min on exposure to heat-inactivated β -galactosidase (113 nM). We also assessed the ability of β -galactosidase to remove the galactopyranose masking group from [Gd-5] by high-pressure liquid chromatography (HPLC) analysis (Figure 3).

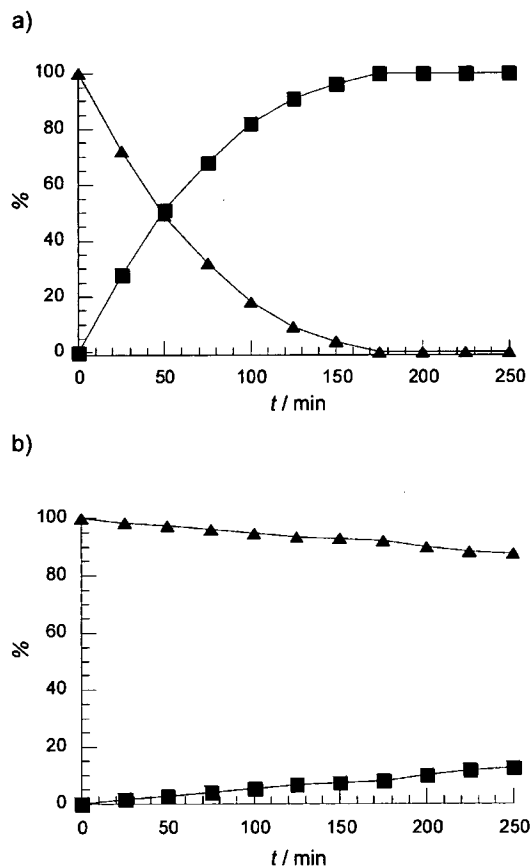


Figure 3. Time course of the conversion of [Gd-5] to [Gd-8]; the distribution of reaction species was quantified by HPLC analysis on the basis of the absorbance at 300 nm. The Gd³⁺ complex, [Gd-5] (0.5 mM) was incubated with: a) β -Galactosidase (113 nM) ([Gd-5]: \blacktriangle , [Gd-8]: \blacksquare) or; b) heat-inactivated β -galactosidase (113 nM) ([Gd-5]: \blacktriangle , [Gd-8]: \blacksquare) at pH 7.4, and 37 °C, in phosphate-buffered saline (PBS) in the presence of 4.5% w/v human serum albumin (HSA).

This HPLC analysis showed that the Gd³⁺ complexes, [Gd-5] and [Gd-8], had distinct retention times, and [Gd-5] was converted into [Gd-8] in the presence of β -galactosidase (113 nM), whereas essentially no change was observed upon the addition of heat-inactivated β -galactosidase (113 nM). The HPLC experiments confirmed the enzymatic processing of [Gd-5] by the β -galactosidase. Thus, [Gd-5] exhibited a β -galactosidase-induced RIME effect, accompanying the removal of the galactopyranose residue of [Gd-5].

The r_1 relaxivity of Gd³⁺ complexes, [Gd-5] and [Gd-8]: The paramagnetic species, Gd³⁺, acts as a catalyst to relax bulk water protons by fast exchange of the coordinated

water with bulk water (inner-sphere contribution). There is also a relaxation increase provided by the Gd^{3+} ion to water molecules which are diffusing close to the Gd^{3+} ion (second-sphere and outer-sphere contributions). The observed longitudinal relaxation rate $(1/T_1)_{obs}$ of the solvent water protons is known to depend on the concentration of Gd^{3+} ions according to Equation (1) :

$$(1/T_1)_{obs} = (1/T_1)_d + r_1[Gd] \quad (1)$$

where $(1/T_1)_{obs}$ is the observed relaxation rate of water protons in the presence of Gd^{3+} , and $(1/T_1)_d$ is the diamagnetic relaxation rate of water protons in the absence of Gd^{3+} . The longitudinal relaxivity value, r_1 , refers to the amount of increase in $1/T_1$ s^{-1} per millimolar concentration of agent (given as mm^{-1} Gd), and $[Gd]$ is the millimolar concentration of Gd^{3+} ions. Therefore, a plot of $(1/T_1)_{obs}$ versus Gd^{3+} concentration would give the r_1 relaxivity as the slope, and the r_1 relaxivity, normally expressed in units of $mm^{-1} sec^{-1}$, reflects the ability of a Gd^{3+} complex to increase relaxation. The water proton relaxivities, r_1 , of **[Gd-5]** and **[Gd-8]** were determined at 20 MHz (0.47 T), at 25 or 37 °C, and are shown in Table 1. In the absence of HSA, the r_1 relaxivities

Table 1. The r_1 relaxivity [$mm^{-1} s^{-1}$] (20 MHz) in PBS with 4.5% HSA or PBS.

Compound	HSA ^[a]		PBS ^[b]	
	25 °C	37 °C	25 °C	37 °C
[Gd-5]	6.34	6.06	5.80	5.35
[Gd-8]	8.76	9.51	4.11	3.87

[a] Human serum albumin (HSA) (4.5% w/v) in phosphate-buffered saline (PBS; 137 mM NaCl, 8.10 mM Na_2HPO_4 , 2.68 mM KCl, 1.47 mM KH_2PO_4 , pH 7.4). [b] PBS only.

of **[Gd-5]** are higher than those of **[Gd-8]** at both 25 and 37 °C. However, in PBS with 4.5% w/v HSA at 25 °C, the r_1 relaxivity of **[Gd-8]** is higher than that of **[Gd-5]** by 38% as a consequence of a higher albumin binding affinity; at 37 °C, where the exchange of Gd^{3+} -bound water molecules is more facile, the r_1 relaxivity of **[Gd-8]** is higher than that of **[Gd-5]** by 57%. From these results, it was considered that the increase of the $1/T_1$ value of **[Gd-5]** in Figure 2 was a consequence of enzymatic cleavage of the galactopyranose residue of **[Gd-5]** by the β -galactosidase activity. Moreover, the r_1 relaxivity of **[Gd-5]** at 20 MHz showed similar values in the absence and the presence of HSA, indicating that **[Gd-5]** hardly interacts with HSA.

Albumin binding study: We investigated the noncovalent interaction between **[Gd-5]** or **[Gd-8]**, and HSA. To demonstrate the extent of relaxation enhancement, the E-titration is shown in Figure 4.^[2,11a] The longitudinal water proton relaxation times T_1 of a 0.1 mM solution of **[Gd-5]** or **[Gd-8]** in PBS with various concentrations of HSA (0–3.35 mM (0–22.5% w/v)) were measured at 20 MHz (0.47 T), 37 °C. The results were expressed in terms of the enhancement factor ϵ^* , that is, the ratio of paramagnetic longitudinal relaxation

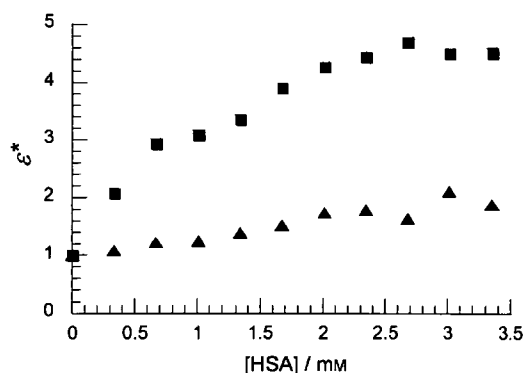


Figure 4. E-titration data for **[Gd-5]** and **[Gd-8]**. ϵ^* versus [human serum albumin (HSA)] in mM, at 37 °C, in phosphate-buffered saline (PBS, pH 7.4) at 20 MHz, 0.47 T. Each solution contains various concentrations of HSA (0–22.5% w/v (=0–3.35 mM)) with 0.1 mM **[Gd-5]** (▲) or **[Gd-8]** (■).

rates ($(1/T_1)_{para}$ [s^{-1}]) in the presence and the absence of HSA were plotted versus increasing HSA concentration at a constant concentration of **[Gd-5]** or **[Gd-8]** (0.1 mM) [Eq. (2)] :

$$\epsilon^* = \frac{(1/T_1)_{obs}^{Alb} - (1/T_1)_{dia}^{Alb}}{(1/T_1)_{obs}^{PBS} - (1/T_1)_{dia}^{PBS}} = \frac{(1/T_1)_{para}^{Alb}}{(1/T_1)_{para}^{PBS}} \quad (2)$$

where the *obs*, *para*, and *dia* subscripts refer to the observed, paramagnetic, and diamagnetic species, respectively, and the *Alb* and *PBS* superscripts refer to “in PBS containing human serum albumin” and “in PBS”, respectively. The longitudinal water proton relaxation times T_1 of aqueous solutions without Gd^{3+} complexes were measured as the diamagnetic contribution. The longitudinal relaxation rate ($1/T_1$ [s^{-1}]) increase of **[Gd-8]** solutions in the presence of HSA was much larger than that of **[Gd-5]** solutions, and did not increase linearly with the concentration of HSA, suggesting protein binding. There was a 1.9- or 4.5-fold increase in the enhancement factor ϵ^* upon binding to HSA for **[Gd-5]** or **[Gd-8]**, respectively. Small parts of these increases in ϵ^* can be ascribed to the misleading apparent amount of water molecules (ref. [4], p. 2342). For example, ≈ 3 mM HSA solution contains more than 20% protein and hence less than 80% water, because of the high molecular weight of HSA. The molar concentration of 1 mmol Gd^{3+} in a liter of 20% w/v HSA is written as 1 mM, but the actual molar concentration would be 1.25 mM. However, the increase of ϵ^* for **[Gd-8]** is sufficiently large even when this problem is taken into consideration. Therefore, the enhancement factor ϵ^* for **[Gd-8]** suggests a high affinity of **[Gd-8]** for the albumin, whereas the slight increase of ϵ^* for **[Gd-5]** can be interpreted as indicating a weak interaction with the albumin.

Further, the binding interaction strengths of **[Gd-5]** and **[Gd-8]** to HSA were calculated by using the above E-titration experimental data.^[2,11b,c,20] The observed longitudinal water proton relaxation rate, $r_{1,obs}$ [s^{-1}] is given by the sum of

three contributions, r_{1p}^F [mm⁻¹ s⁻¹], r_{1p}^B [mm⁻¹ s⁻¹], and r_{1dia} [s⁻¹]:

$$r_{1obs} - r_{1dia} = (r_{1p}^F[Gd] + r_{1p}^B[Gd-HSA]) \times 1000 \quad (3)$$

where r_{1p}^F and r_{1p}^B are the r_1 relaxivity [mm⁻¹ s⁻¹] of the Gd³⁺ complex and of the paramagnetic macromolecular, Gd³⁺ complex-HSA adduct, respectively, and r_{1dia} [s⁻¹], is the diamagnetic contribution of the observed longitudinal water proton relaxation rate r_{1obs} [s⁻¹], at 20 MHz, 37 °C. [Gd], in M, is the concentration of the Gd³⁺ complex, and [Gd-HSA], in M, is the concentration of the Gd³⁺ complex-HSA adduct. The determination of the binding parameter nK_A [M⁻¹] (K_A : association constant; n : number of independent binding sites on the protein) for the equilibrium:



is possible through the following equations:

$$K_A = \frac{[Gd-HSA]}{[Gd] \cdot [n \cdot HSA]} \quad (5)$$

By combining Equations (3) and (5) we obtain Equation (6), which allows the nonlinear fitting of the experimental data:

$$r_{1obs} - r_{1d} = \left(r^F \cdot B + (r^B - r^F) \times \frac{K_A A + K_A B + 1 - \sqrt{(K_A A + K_A B + 1)^2 - 4K_A^2 AB}}{2K_A} \right) \times 1000 \quad (6)$$

where A and B [both in M], are the total molar concentrations of HSA and the Gd³⁺ complex, respectively. The fitting of the experimental data into Equation (6) provided an assessment of the binding strength, nK_A [M⁻¹], and the r_1 relaxivity [mm⁻¹ s⁻¹], of the macromolecular adduct (r_1^B [mm⁻¹ s⁻¹]) (see the Supporting Information). The interaction strength of [Gd-8] with HSA was fairly strong ($nK_A = 7.0 \times 10^2$ M⁻¹) and the r_1 relaxivity of the paramagnetic macromolecular [Gd-8]-HSA adduct (r_1^B) was 20 mm⁻¹ s⁻¹, at 20 MHz and 37 °C, whereas the interaction of [Gd-5] with HSA was rather weak ($nK_A < 1.0 \times 10^2$ M⁻¹).

Further, we examined whether various other species of albumins, such as, rat, bovine, and rabbit serum albumins, could serve as host macromolecules for [Gd-8], like HSA. When [Gd-5] (0.1 mM) was incubated with β -galactosidase (1.13 μ M), at 37 °C, for 30 min, in PBS, with 4.5% w/v human, rat, bovine, or rabbit serum albumin, all solutions showed similar decreases of the longitudinal relaxation time (T_1) of water protons (see Supporting Information).

Time-resolved luminescence and UV/Vis absorption spectra of [Tb-5] and [Tb-8]: The chemical properties of [Gd-5] and [Gd-8] were further assessed by analyzing the luminescence and chemical properties of the terbium trivalent ion (Tb³⁺) complexes of chelator 5 and 8, [Tb-5] and [Tb-8] (Figure 5). Lanthanide complexes, in particular complexes of Tb³⁺ and Eu³⁺ (the europium trivalent ion), have advanced

tageous spectroscopic characteristics, such as, long luminescence lifetimes of the order of milliseconds, narrow emission peaks, a large Stoke's shift of > 150 nm, and excellent water solubility.^[21] This extremely long luminescence lifetime of lanthanide ions allows a time-resolved detection procedure to be employed, because typical fluorescence lifetimes are in the nanosecond region; that is, a delay time is set between the excitation pulse and the measurement of the lanthanide luminescence, during which the background fluorescence and scattered light decay to negligible levels.^[22] Therefore, time-resolved luminescence measurements offer a better signal-to-noise ratio, and the lanthanide luminescence has been exploited in a number of useful detection systems for time-resolved assays in the fields of medicine, biotechnology, and biological science.^[23] We prepared [Tb-5] and [Tb-8] as homologues of [Gd-5] and [Gd-8], because the Tb³⁺ ion possesses the same charge as Gd³⁺, as well as similar ionic radius and coordination chemistry to the Gd³⁺ ion.^[24] The synthetic schemes for [Tb-5] and [Tb-8] and details of the chemical characterization of compounds are provided in the Supporting Information. As regards the metal-based luminescence properties, 25 μ M aqueous solutions of [Tb-5] and [Tb-8] (in 100 mM HEPES buffer; pH 7.4) were relatively brightly luminescent upon excitation at 254 nm with a TLC plate reader lamp, and these emissions of [Tb-5] and [Tb-8] were observed with the naked eye (see Supporting Information).

First, the UV/Vis absorption spectrum of [Tb-5] (50 μ M) and [Tb-8] (50 μ M) was measured in 100 mM HEPES buffer at pH 7.4, 25 °C. The absorption spectra of [Tb-5] and [Tb-8] were similar, that is, [Tb-5] showed a λ_{max} at 279 nm tailing out to 330 nm, and [Tb-8] showed a λ_{max} at 281 nm tailing to 330 nm (Figure 6a). These absorption spectra can be mainly ascribed to the biphenyl substituent, because the bands observed in Tb³⁺ absorption spectra are usually very weak, that is, molar absorption coefficients (ϵ) of lanthanide(III) ions are usually < 1 dm³ mol⁻¹ cm⁻¹.^[21] Second, the time-resolved luminescence spectrum of [Tb-5] (50 μ M) or [Tb-8] (50 μ M) was measured in 100 mM HEPES buffer (pH 7.4) upon excitation of the biphenyl substituent (excitation at 280 nm) for both [Tb-5] and [Tb-8]. The time-resolved luminescence spectra of [Tb-5] and [Tb-8], with a delay time of 50 μ s, displayed four bands (490, 545, 586, and 622 nm), arising from transitions from the emissive ⁵D₄ state to the ground-state manifolds, ⁷F₆, ⁷F₅, ⁷F₄, and ⁷F₃, respectively (Figure 6b).^[21a,b] On the basis of the above spectroscopic results, the biphenyl substituent, which is the albumin-binding group, serves as a sensitizing chromophore for Tb³⁺ in the luminescent Tb³⁺ complexes, [Tb-5] and [Tb-8].

The time-resolved luminescence spectra, with a delay time of 50 μ sec, of [Tb-5] (50 μ M) were measured in 100 mM HEPES buffer at pH 7.4, 25 °C excited at the absorbance maximum (λ_{max}) wavelength of the biphenyl group (280 nm) during the enzyme (β -galactosidase) reaction. Addition of β -

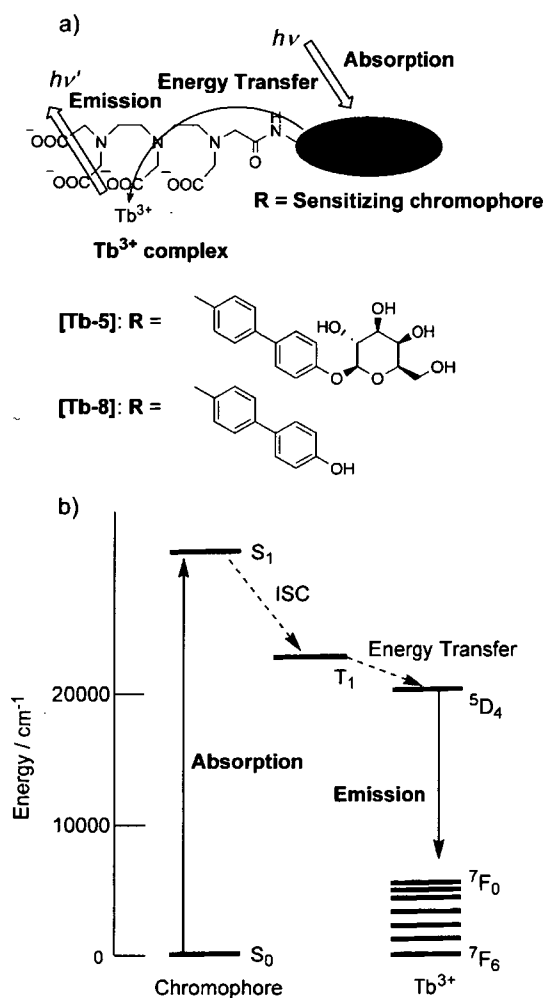


Figure 5. a) Structures of Tb³⁺ complexes, [Tb-5] and [Tb-8], and schematic view of a chromophore incorporated into a terbium emitter. The emission from Tb³⁺ after excitation of the sensitizing chromophore on Tb³⁺ complexes, [Tb-5] and [Tb-8], is shown. b) The general chromophore-to-terbium-ion sensitization process. Light absorption and lowest-lying singlet excited state (S₁) formation at the sensitizing chromophore are followed by intersystem crossing (ISC), resulting in population of the triplet excited state (T₁) of the sensitizing chromophore. Subsequent chromophore-to-Tb³⁺ energy transfer leads to a metal-centered emission, which is derived from transitions from Tb³⁺-emitting states to the relevant ground states.

galactosidase (113 nm) to an aqueous solution of [Tb-5] resulted in a decrease in the luminescence of Tb³⁺ as shown in Figure 6c. The luminescence intensity at 545 nm of the [Tb-5] solution decreased by about 43% of the initial luminescence intensity when β-galactosidase was added. HPLC monitoring of the conversion of [Tb-5] into [Tb-8] confirmed the removal of the galactopyranose residue of [Tb-5] with a concomitant luminescence decrease (data not shown). The kinetic parameters for the enzyme reaction of [Tb-5] with β-galactosidase were determined by measuring the luminescence change of [Tb-5], because it is well known that the linear relationship of the longitudinal relaxation

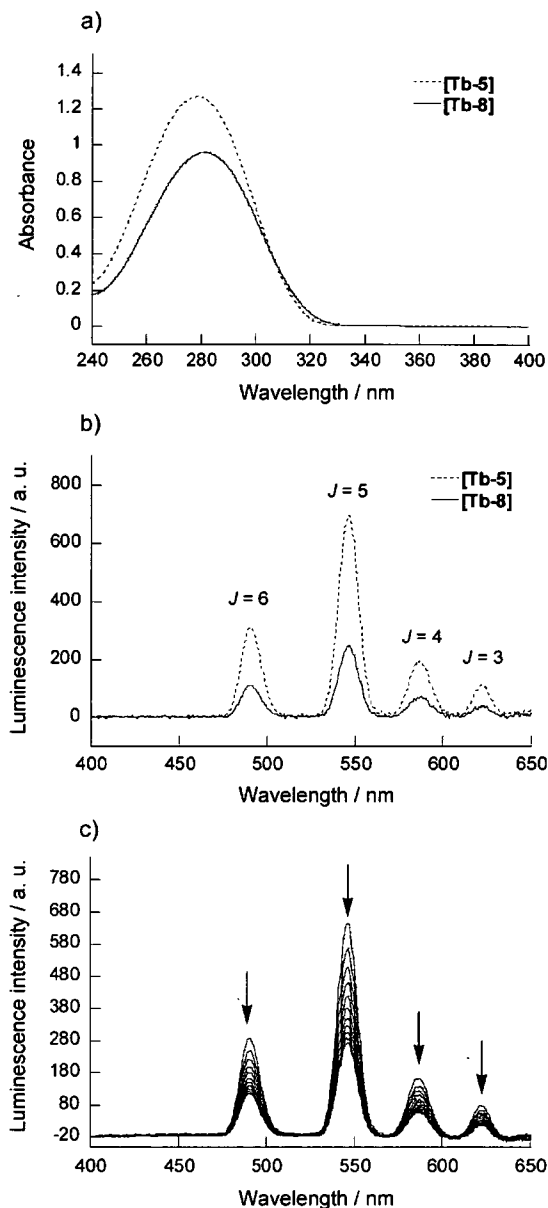


Figure 6. Spectroscopic characteristics of solutions of [Tb-5] and [Tb-8] upon addition of β-galactosidase. a) Absorbance spectra of 50 μM aqueous solution (100 mM HEPES buffer, pH 7.4) of [Tb-5] and [Tb-8] at 25 °C ([Tb-5]: ---, [Tb-8]: —). b) Time-resolved emission spectra (excitation at 280 nm) of [Tb-5] and [Tb-8] (50 μM) ([Tb-5]: ---, [Tb-8]: —). These spectra were measured in 100 mM HEPES buffer at pH 7.4 and 25 °C by using a delay time of 50 μs and a gate time of 1.00 ms. The bands arise from 5D₄→7F_J transitions; the J values of the bands are labeled. c) Time-resolved emission spectra (excitation at 280 nm) of [Tb-5] (50 μM) after the addition of β-galactosidase (113 nm) in 100 mM HEPES buffer (pH 7.4) at 25 °C. Time-resolved emission spectra of [Tb-5] were measured every 10 min (0 ≈ 100 min) after the addition of β-galactosidase.

rates, $1/T_1$, of the water protons is valid only if the concentration of the paramagnetic species, Gd³⁺, is at the level of mmol or submmol per kilogram of solvent (millimolality or submillimolality),^[2] whereas for the determination of the ki-

netic parameters, the β -galactosidase substrate concentration should be in the range of several μM \approx several hundred μM . Kinetic parameters K_m and k_{cat} were determined by direct fitting of the initial velocity versus substrate concentration data to the Michaelis–Menten equation (see Supporting Information). The values of K_m , k_{cat} , and k_{cat}/K_m of **[Tb-5]** for β -galactosidase were 81.6 μM , 2.7 s^{-1} , and 33.1 $\text{mM}^{-1}\text{s}^{-1}$, respectively. For reference, the values for *o*-nitrophenyl β -D-galactoside (ONPG) and phenyl β -D-galactoside (PG) for β -galactosidase have been reported to be $K_m=100$ and 90 μM , $k_{\text{cat}}=600$ and 35 s^{-1} , $k_{\text{cat}}/K_m=6000$ and 389 $\text{mM}^{-1}\text{s}^{-1}$, respectively.^[25] The reactivity of **[Tb-5]** for β -galactosidase is likely to be sufficient for the detection of enzyme activity in biological systems, on the basis of the kinetic parameters of ONPG and PG, and the experimental data from refs. [10a,b] and [26]. The k_{cat}/K_m value of **[Tb-5]** is probably determined by the structure of the biphenyl group which is the albumin binding moiety,^[27] so it should be possible to modulate the k_{cat}/K_m value of **[Tb-5]** for β -galactosidase by modifying the structure of the albumin binding moiety. Moreover, the reactivity of **[Tb-5]** with β -galactosidase appears to be much higher than that of the β -galactosidase-activated MRI probe which was reported by Meade and co-workers.^[10b]

Luminescence and chemical properties of [Tb-5] and [Tb-8]: We further investigated in the luminescence and chemical properties of **[Tb-5]** and **[Tb-8]**, and these properties are summarized in Table 2. The luminescence quantum yields (φ) of **[Tb-5]** and **[Tb-8]** were 0.4 and 0.2%, respectively, under air-equilibrated conditions (Table 2). This result corresponds to the phenomenon of the luminescence intensity decrease of **[Tb-5]** in the presence of β -galactosidase. These luminescence quantum yields are relatively low, as compared with those reported for highly luminescent lanthanide complexes,^[23f,g,k] but they are sufficiently large for luminescence detection, as described above. Measurement of the decay rate constants of the Tb^{3+} excited state for **[Tb-5]** and **[Tb-8]** were carried out in both H_2O and D_2O . The luminescence lifetimes of **[Tb-5]** and **[Tb-8]** were found to be 0.77 and 0.23 ms in H_2O ($\tau_{\text{H}_2\text{O}}$), and 1.03 and 0.43 ms in D_2O ($\tau_{\text{D}_2\text{O}}$), respectively (Table 2). The luminescence lifetime of **[Tb-8]** which is shorter than that of **[Tb-5]** may cause the difference of luminescence intensity between **[Tb-5]** and **[Tb-8]**. These luminescence lifetimes also indicated that the

Table 2. Luminescence and chemical properties.

Compound	φ [%] ^[a]	$\tau_{\text{H}_2\text{O}}$ [ms] ^[b]	$\tau_{\text{D}_2\text{O}}$ [ms] ^[c]	q ^[d]
[Tb-5]	0.4	0.77	1.03	1.35
[Tb-8]	0.2	0.23	0.43	– ^[e]

[a] Quantum yields were calculated by using quinine sulfate ($\varphi=0.546$ in 1N H_2SO_4)^[28] as a standard, and measured in 100 mM HEPES buffer; pH 7.4. [b] In H_2O -based buffer (100 mM HEPES buffer, pH 7.4). [c] In D_2O -based buffer (100 mM HEPES buffer, pH 7.4). [d] The q values were estimated by using the equation $q^{\text{Tb}}=5(1/\tau_{\text{H}_2\text{O}}-1/\tau_{\text{D}_2\text{O}}-0.06)$, which allows for the contribution of unbound water molecules.^[29a,b] [e] The chelated q value of **[Tb-8]** was extremely large (9.8), and this value seems not to reflect the number of coordinated water molecules to the centered metal ion, Tb^{3+} . Other factors may account for this extremely large q value.

numbers of coordinated water molecules (q values) at the metal center, Tb^{3+} , were 1.35 and 9.8 for **[Tb-5]** and **[Tb-8]**, respectively (Table 2), according to Equation (7).^[29a,b]

Number of water molecules :

$$q^{\text{Tb}} = 5(1/\tau_{\text{H}_2\text{O}} - 1/\tau_{\text{D}_2\text{O}} - 0.06) \quad (7)$$

The q value of **[Tb-5]** is reasonable, considering the experimental data of longitudinal relaxation time (T_1) and long-lived luminescence measurements in this paper, and indicates that **[Tb-5]** has approximately one water molecule coordinated to the chelated Tb^{3+} . Further, in general, the lanthanide trivalent ion (Ln^{3+}) (such as, Eu^{3+} , Gd^{3+} , Tb^{3+}) complexes of DTPA-monoamide or DTPA-bisamide derivatives, which have a coordination number of eight for Ln^{3+} , have approximately one metal-bound water molecule.^[4,21 a,23f,30] However, the q value of **[Tb-8]** was extremely large, 9.8, showing inconsistency with other experimental data herein, and therefore this calculated value seems not to reflect the number of water molecules coordinated to the central metal ion, Tb^{3+} . Other factors could account for this extremely large q value of **[Tb-8]**, and the mechanism of this abnormal feature of **[Tb-8]** is now under investigation.

Conclusion

The Gd^{3+} complex **[Gd-5]** is the first RIME-based β -galactosidase-activated MRI contrast agent, and our design strategy should be applicable to a range of new types of β -galactosidase-activated MRI contrast agents, which may possess novel chemical characteristics, such as, various reactivity with β -galactosidase, specific biodistribution in living specimens and cells, differing extent of r_1 relaxivity change, and so on. This bioactive MRI contrast agent **[Gd-5]** should be useful for studies on the gene expression of lacZ in biological systems.^[1a,8,10]

Experimental Section

All reagents were purchased from Tokyo Kasei Kogyo Co. Ltd. (Japan), Wako Pure Chemical Industries Ltd. (Japan), or Aldrich Chemical Co. Inc. (St. Louis, MO), and were used directly without further purification. All solvents were used after distillation. β -Galactosidase [EC 3.2.1.23] Sigma cat G 6008 (Grade VI: From *Escherichia coli*), HSA (human serum albumin, 97–99%) Sigma cat A 9511 (1 \times crystallized and lyophilized), albumin from rat serum Sigma cat A 6272, BSA (bovine serum albumin) Sigma cat A 7906 (minimum 98% electrophoresis), and albumin from rabbit serum Sigma cat A 0764 (ca. 99% agarose gel electrophoresis) were purchased from Sigma. Dulbecco's phosphate-buffered saline (D-PBS(–)) Sigma cat 14190–136 was purchased from GIBCO, and was used as phosphate-buffered saline (PBS). Silica gel column chromatography was performed by using BW-300, and Chromatorex-ODS (both from Fuji Silysia Chemical Ltd., Japan). Amberlite IR-120 Plus(H) was purchased from ICN Biomedicals, Inc. (USA). Chelex 100 resin (100–200 mesh, sodium form) was purchased from Bio-Rad Laboratories (USA). **Instruments:** ¹H and ¹³C NMR spectra were recorded by using a JEOL JNM-LA300 spectrometer. Mass spectra were measured by using a JEOL-T100LC AccuTOF mass spectrometer (ESI⁺ and ESI⁻). HPLC

purification was performed on a reversed-phase column, Inertsil Prep-ODS 30 mm × 250 mm (GL Sciences, Inc. (Tokyo, Japan)) fitted on a Jasco PU-1587 system. Measurements of longitudinal water proton relaxation times (T_1) were made by using an NMR analyzer operating at 20 MHz, 0.47 T (Minispec mq20, Bruker). Time-resolved luminescence spectra were recorded by using a Perkin-Elmer LS-55 (Beaconsfield, Buckinghamshire, England). UV/Vis spectra were obtained by using a Shimadzu UV-1650PC (Tokyo, Japan). Normal fluorescence spectra were measured by using a Hitachi F4500 spectrofluorometer (Tokyo, Japan). Aqueous solutions of Tb³⁺ complexes illuminated at 254 nm were photographed by using a Handy UV lamp (Handy UV Lamp, SLUV-4, AS ONE Co., Japan) (see Supporting Information).

Relaxation-time measurements: The longitudinal water proton relaxation times, T_1 , of aqueous solutions of the Gd³⁺ complex [Gd-5] or [Gd-8] were measured in phosphate-buffered saline (PBS, Dulbecco's phosphate-buffered saline, pH 7.4) or PBS with albumin at 20 MHz, 0.47 T (Minispec mq20, Bruker). The values of T_1 were measured from 10 points generated by using the standard inversion-recovery procedure. The r_1 relaxivity [mM⁻¹s⁻¹] of [Gd-5] or [Gd-8] was determined from the slope of the plot of $1/T_1$ versus [[Gd-5]] or [[Gd-8]] (0.25, 0.325, 0.4, and 0.475 mM) in PBS or PBS with 4.5% w/v HSA at 25°C or 37°C.

HPLC analysis: The transformation of [Gd-5] or [Tb-5] to [Gd-8] or [Tb-8] was monitored by using HPLC analysis. The HPLC analysis for the transformation of [Gd-5] to [Gd-8] was performed on a reversed-phase column (Inertsil ODS-3 4.6 × 250 mm (GL Sciences)); eluent, a 20-min linear gradient, from 0 to 80% solvent B (solvent A, 0.1 M triethylammonium acetate (pH 6.5); solvent B, acetonitrile/H₂O 4:1); flow rate, 1.0 mL min⁻¹; UV 300 nm). The retention times of [Gd-5] and [Gd-8] under these conditions were 9.1 and 11.5 min, respectively. The HPLC analysis to measure the transformation of [Tb-5] to [Tb-8] was performed by using a reversed-phase column (Inertsil ODS-3 4.6 × 250 mm (GL Sciences)); eluent, a 70-min linear gradient, from 10 to 80% solvent B (solvent A, 0.1 M triethylammonium acetate (pH 6.5); solvent B, acetonitrile/H₂O 4:1); flow rate, 1.0 mL min⁻¹; UV 280 nm). The retention times of [Tb-5] and [Tb-8] under these conditions were 7.7 and 14.9 min, respectively.

T_1 relaxation time measurements of [Gd-5] with β -galactosidase: The longitudinal relaxation T_1 times were measured for [Gd-5] in the presence of β -galactosidase (113 nm) or heat-inactivated β -galactosidase (10 min at 80°C) at 113 nm, with 4.5% w/v HSA in PBS (pH 7.4), at 20 MHz, 0.47 T, at 37°C. The concentration of β -galactosidase was calculated based on a monomer of $M_w = 116.3$ kDa.^[31] On HPLC analysis of the reaction mixture, only two peaks of [Gd-5] and [Gd-8] were detected at 300 nm.

Albumin binding study: The T_1 relaxation times of [Gd-5] (0.1 mM) or [Gd-8] (0.1 mM) were measured in PBS (pH 7.4) with various concentrations of HSA (0, 0.335, 0.67, 1.005, 1.34, 1.675, 2.01, 2.345, 2.68, 3.015, and 3.35 mM). The concentrations of HSA were determined on the basis of 4.5% w/v = ≈ 0.67 mM.^[4,11a]

Comparison of various species of serum albumins: The longitudinal water proton relaxation times T_1 of [Gd-5] or [Gd-8] were measured at 37°C in PBS (pH 7.4) in the presence of 4.5% w/v serum albumin from four different species (human, rat, bovine, and rabbit) in the presence or absence of β -galactosidase (1.13 μ M).

UV/Vis absorption spectral measurements: The absorption spectra of [Tb-5] (50 μ M) or [Tb-8] (50 μ M) were measured at 25°C in aqueous solution buffered to pH 7.4 (100 mM HEPES buffer).

Time-resolved luminescence spectral measurements: The time-resolved luminescence spectra of [Tb-5] or [Tb-8] (50 μ M, respectively) were measured in 100 mM HEPES buffer at pH 7.4, 25°C (excitation at 280 nm for [Tb-5] and [Tb-8], respectively). The slit width was 10 nm for both excitation and emission. A delay time of 50 μ s and a gate time of 1.00 ms were used.

Kinetic studies: Kinetic parameters K_m and k_{cat} were determined by direct fitting of the initial velocity versus substrate ([Tb-5]) concentration data to the Michaelis-Menten equation as shown in the Supporting Information. The initial velocities were determined by monitoring the de-

crease of the Tb³⁺ luminescence of [Tb-5] solutions at 37°C in PBS (pH 7.4) (excitation 280 nm, emission 545 nm) with a Hitachi F4500 spectrofluorometer, in the presence of β -galactosidase (151 nm) and various concentrations of [Tb-5] (5, 10, 20, 40, 80, and 160 μ M). The slit width was 5 nm for both excitation and emission. The photomultiplier voltage was 700 V.

Quantum yield measurements: The luminescence spectra were measured with a Hitachi F4500 spectrofluorometer. The slit width was 2.5 nm for both excitation and emission. The photomultiplier voltage was 700 V. The luminescence spectra of [Tb-5] or [Tb-8] were measured in 100 mM HEPES buffer at pH 7.4, 25°C, with irradiation at 280 nm. The quantum yields of Tb³⁺ complexes were evaluated by using a relative method with reference to a luminescence standard, quinine sulfate ($\phi = 0.546$ in 1 N H₂SO₄).^[28] The quantum yields of Tb³⁺ complexes can be expressed by Equation (9)^[32]:

$$\Phi_x/\Phi_{st} = [A_{st}/A_x][n_x^2/n_{st}^2][D_x/D_{st}] \quad (8)$$

where Φ is the quantum yield (subscript "st" stands for the reference and "x" for the sample), A is the absorbance at the excitation wavelength, n is the refractive index, and D is the peak area (on an energy scale) of the luminescence spectra. The samples and the reference were excited at the same wavelength (280 nm). The sample and the reference absorbance at the excitation wavelength were kept as low as possible to avoid fluorescence errors ($A_{exc} < 0.05$).

Luminescence lifetime measurements: The luminescence lifetimes of the Tb³⁺ complexes were recorded on a Perkin-Elmer LS-55 instrument. The data were collected with a 10- μ s resolution in H₂O (100 mM HEPES buffer at pH 7.4) and D₂O (100 mM HEPES buffer at pD 7.4, based on the equation pD = pH + 0.40^[33]) at 25°C, and fitted to a single-exponential curve obeying Equation (9):

$$I = I_0 \exp(-t/\tau) \quad (9)$$

where I_0 and I are the luminescence intensities at the time $t=0$ and time t , respectively, and τ is the luminescence emission lifetime. Lifetimes were obtained by monitoring the emission intensity at 545 nm (excitation at 280 nm).

Acknowledgement

This work was supported by the Ministry of Education, Culture, Sports, Science and Technology of Japan (Grants for The Advanced and Innovative Research Program in Life Sciences, 16370071 and 16659003 to T.N., 15681012, 17035019, 17036012, 017048006, and 17651119 to K.K.). T.N. was also supported by the Hoh-ansha Foundation. K.K. was also supported by the Sankyo Foundation, by the Kanagawa Academy of Science, and by the Shimadzu Foundation. K.H. was the recipient of Research Fellowships of the Japan Society for the Promotion of Science for Young Scientists. We thank Professor Haruhiko Bito for valuable suggestions.

- [1] a) G. Genove, U. DeMarco, H. Xu, W. F. Goins, E. T. Ahrens, *Nat. Med.* **2005**, *11*, 450–454; b) K. H. Thompson, C. Orvig, *Science* **2003**, *300*, 936–939; c) K. Nakahara, T. Hayashi, S. Konishi, Y. Miyashita, *Science* **2002**, *295*, 1532–1536; d) H. Degani, V. Gusic, D. Weinstein, S. Fields, S. Strano, *Nat. Med.* **1997**, *3*, 780–782; e) R. E. Jacobs, S. E. Fraser, *Science* **1994**, *263*, 681–684; f) J. C. Frias, K. J. Williams, E. A. Fisher, Z. A. Fayad, *J. Am. Chem. Soc.* **2004**, *126*, 16316–16317.
- [2] A. E. Merbach, É. Tóth, *The Chemistry of Contrast Agents in Medical Magnetic Resonance Imaging*, Wiley, New York, **2001**.

- [3] a) S. Aime, M. Botta, M. Fasano, E. Terreno, *Acc. Chem. Res.* **1999**, *32*, 941–949; b) S. Aime, M. Botta, M. Fasano, E. Terreno, *Chem. Soc. Rev.* **1998**, *27*, 19–29.
- [4] P. Caravan, J. J. Ellison, T. J. McMurry, R. B. Lauffer, *Chem. Rev.* **1999**, *99*, 2293–2352.
- [5] V. M. Runge, D. Y. Gelblum, M. L. Pacetti, F. Carolan, G. Heard, *Radiology* **1990**, *177*, 393–400.
- [6] a) M. P. Lowe, *Aust. J. Chem.* **2002**, *55*, 551–556; b) L. Thunus, R. Lejeune, *Coord. Chem. Rev.* **1999**, *184*, 125–155; c) V. Comblin, D. Gilsoul, M. Hermann, V. Humblet, V. Jacques, M. Mesbahi, C. Sauvage, J. F. Desreux, *Coord. Chem. Rev.* **1999**, *185–186*, 451–470; d) M. K. Thompson, B. Misselwitz, L. S. Tso, D. M. J. Doble, H. Schmitt-Willich, K. N. Raymond, *J. Med. Chem.* **2005**, *48*, 3874–3877; e) V. C. Pierre, M. Botta, K. N. Raymond, *J. Am. Chem. Soc.* **2005**, *127*, 504–505; f) H. Kato, Y. Kanazawa, M. Okumura, A. Tanimaka, T. Yokawa, H. Shinohara, *J. Am. Chem. Soc.* **2003**, *125*, 4391–4397; g) M. Mikawa, H. Kato, M. Okumura, M. Narazaki, Y. Kanazawa, N. Miwa, H. Shinohara, *Bioconjugate Chem.* **2001**, *12*, 510–514; h) A. Accardo, D. Tesaro, P. Roscigno, E. Gianolio, L. Paduano, G. D'Errico, C. Pedone, G. Morelli, *J. Am. Chem. Soc.* **2004**, *126*, 3097–3107; i) J. Lee, M. J. Zylka, D. J. Anderson, J. E. Burdette, T. K. Woodruff, T. J. Meade, *J. Am. Chem. Soc.* **2005**, *127*, 13164–13166.
- [7] a) T. J. Meade, A. K. Taylor, S. R. Bull, *Curr. Opin. Neurobiol.* **2003**, *13*, 597–602; b) J. A. Duimstra, F. J. Femia, T. J. Meade, *J. Am. Chem. Soc.* **2005**, *127*, 12847–12855; c) W. Li, S. E. Fraser, T. J. Meade, *J. Am. Chem. Soc.* **1999**, *121*, 1413–1414; d) W. Li, G. Parigi, M. Fragai, C. Luchinat, T. J. Meade, *Inorg. Chem.* **2002**, *41*, 4018–4024; e) S. Zhang, K. Wu, A. D. Sherry, *Angew. Chem.* **1999**, *111*, 3382–3384; *Angew. Chem. Int. Ed.* **1999**, *38*, 3192–3194; f) N. Raghunand, C. Howison, A. D. Sherry, S. Zhang, R. J. Gillies, *Magn. Reson. Med.* **2003**, *49*, 249–257; g) É. Tóth, R. D. Bolskar, A. Borel, G. González, L. Helm, A. E. Merbach, B. Sitharaman, L. J. Wilson, *J. Am. Chem. Soc.* **2005**, *127*, 799–805; h) M. Mikawa, N. Miwa, M. Bräutigam, T. Akaike, A. Maruyama, *J. Biomed. Mater. Res.* **2000**, *49*, 390–395; i) M. Mikawa, T. Yokawa, N. Miwa, M. Brautigam, T. Akaike, A. Maruyama, *Acad. Radiol.* **2002**, *9*, S109–S111; j) K. E. Løkling, R. Skurtveit, A. Bjørnerud, S. L. Fosshem, *Magn. Reson. Med.* **2004**, *51*, 688–696; k) S. Aime, M. Botta, E. Gianolio, E. Terreno, *Angew. Chem.* **2000**, *112*, 763–766; *Angew. Chem. Int. Ed.* **2000**, *39*, 747–750; l) K. Hanaoka, K. Kikuchi, Y. Urano, M. Narazaki, T. Yokawa, S. Sakamoto, K. Yamaguchi, T. Nagano, *Chem. Biol.* **2002**, *9*, 1027–1032; m) K. Hanaoka, K. Kikuchi, Y. Urano, T. Nagano, *J. Chem. Soc. Perkin Trans. 2* **2001**, 1840–1843; n) R. Trokowsky, S. Zhang, A. D. Sherry, *Bioconjugate Chem.* **2004**, *15*, 1431–1440.
- [8] a) D. Högemann, J. P. Babilion, *Eur. J. Nucl. Med.* **2002**, *29*, 400–408; b) R. Weissleder, A. Moore, R. Mahmood, R. Bhorade, H. Benveniste, E. A. Chiocca, J. P. Babilion, *Nat. Med.* **2000**, *6*, 351–354.
- [9] D. J. Spergel, U. Krüth, D. R. Shimshek, R. Sprengel, P. H. Seeburg, *Prog. Neurobiol.* **2001**, *63*, 673–686.
- [10] a) A. Y. Louie, M. M. Hüber, E. T. Ahrens, U. Rothbächer, R. Moats, R. E. Jacobs, S. E. Fraser, T. J. Meade, *Nat. Biotechnol.* **2000**, *18*, 321–325; b) R. A. Moats, S. E. Fraser, T. J. Meade, *Angew. Chem.* **1997**, *109*, 749–752; *Angew. Chem. Int. Ed. Engl.* **1997**, *36*, 726–728; c) M. M. Alauddin, A. Y. Louie, A. Shahinian, T. J. Meade, P. S. Conti, *Nucl. Med. Biol.* **2003**, *30*, 261–265.
- [11] a) P. Cravan, N. J. Cloutier, M. T. Greenfield, S. A. McDermid, S. U. Dunham, J. W. M. Bulte, J. C. Amedeo, Jr., R. J. Looby, R. M. Supkowski, W. Dew. Horrocks, Jr., T. J. McMurry, R. B. Lauffer, *J. Am. Chem. Soc.* **2002**, *124*, 3152–3162; b) S. Amie, E. Gianolio, E. Terreno, G. B. Giovenzana, R. Pagliarin, M. Sisti, G. Palmisano, M. Botta, M. P. Lowe, D. Parker, *J. Biol. Inorg. Chem.* **2000**, *5*, 488–497; c) S. Aime, M. Botta, S. G. Crich, G. B. Giovenzana, R. Pagliarin, M. Piccinini, M. Sisti, E. Terreno, *J. Biol. Inorg. Chem.* **1997**, *2*, 470–479.
- [12] R. B. Lauffer, T. J. McMurry, S. O. Dunham, D. M. Scott, D. J. Parmelee, S. Dumas, *PCT Int. Appl. WO 9736619*, **1997**.
- [13] A. L. Nivorozhkin, A. F. Kolodziej, P. Caravan, M. T. Greenfield, R. B. Lauffer, T. J. McMurry, *Angew. Chem.* **2001**, *113*, 2987–2990; *Angew. Chem. Int. Ed.* **2001**, *40*, 2903–2906.
- [14] L. M. De León-Rodríguez, A. Ortiz, A. L. Weiner, S. Zhang, Z. Kovacs, T. Kodadek, A. D. Sherry, *J. Am. Chem. Soc.* **2002**, *124*, 3514–3515.
- [15] P. L. Anelli, I. Bertini, M. Fragai, L. Lattuada, C. Luchinat, G. Parigi, *Eur. J. Inorg. Chem.* **2000**, 625–630.
- [16] L. Josephson, J. M. Perez, R. Weissleder, *Angew. Chem.* **2001**, *113*, 3304–3306; *Angew. Chem. Int. Ed.* **2001**, *40*, 3204–3206.
- [17] J. W. Chen, W. Pham, R. Weissleder, A. Bogdanov, Jr., *Magn. Reson. Med.* **2004**, *52*, 1021–1028.
- [18] M. Zhao, L. Josephson, Y. Tang, R. Weissleder, *Angew. Chem.* **2003**, *115*, 1413–1416; *Angew. Chem. Int. Ed.* **2003**, *42*, 1375–1378.
- [19] S. Aime, M. Chiaussa, G. Digilio, E. Gianolio, E. Terreno, *J. Biol. Inorg. Chem.* **1999**, *4*, 766–774.
- [20] S. Aime, M. Botta, M. Fasano, S. G. Crich, E. Terreno, *J. Biol. Inorg. Chem.* **1996**, *1*, 312–319.
- [21] a) D. Parker, J. A. G. Williams, *J. Chem. Soc. Dalton Trans.* **1996**, 3613–3628; b) D. Parker, *Coord. Chem. Rev.* **2000**, *205*, 109–130; c) G. R. Choppin, D. R. Peterman, *Coord. Chem. Rev.* **1998**, *174*, 283–299.
- [22] P. R. Selvin, T. M. Rana, J. E. Hearst, *J. Am. Chem. Soc.* **1994**, *116*, 6029–6030.
- [23] a) I. Hemmilä, S. Webb, *Drug Discovery Today* **1997**, *2*, 373–381; b) A. J. Kolb, P. V. Kaplita, D. J. Hayes, Y. W. Park, C. Pernell, J. S. Major, G. Mathis, *Drug Discovery Today* **1998**, *3*, 333–342; c) V. Laitala, I. Hemmilä, *Anal. Chem.* **2005**, *77*, 1483–1487; d) J. Karvinen, V. Laitala, M. L. Mäkinen, O. Mulari, J. Tamminen, J. Hermonen, P. Hurskainen, I. Hemmilä, *Anal. Chem.* **2004**, *76*, 1429–1436; e) Y. Koshi, E. Nakata, I. Hamachi, *ChemBioChem* **2005**, *6*, 1349–1352; f) K. Hanaoka, K. Kikuchi, H. Kojima, Y. Urano, T. Nagano, *J. Am. Chem. Soc.* **2004**, *126*, 12470–12476; g) N. Weibel, L. J. Charbonnière, M. Guardigli, A. Roda, R. Ziessel, *J. Am. Chem. Soc.* **2004**, *126*, 4888–4896; h) M. K. Johansson, R. M. Cook, J. Xu, K. N. Raymond, *J. Am. Chem. Soc.* **2004**, *126*, 16451–16455; i) Z. Lin, M. Wu, M. Schäferling, O. S. Wolfbeis, *Angew. Chem.* **2004**, *116*, 1767–1770; *Angew. Chem. Int. Ed.* **2004**, *43*, 1735–1738; j) K. Lee, V. Dzubeck, L. Latshaw, J. P. Schneider, *J. Am. Chem. Soc.* **2004**, *126*, 13616–13617; k) S. Mameri, L. J. Charbonnière, R. F. Ziessel, *Inorg. Chem.* **2004**, *43*, 1819–1821; l) C. Li, G. L. Law, W. T. Wong, *Org. Lett.* **2004**, *6*, 4841–4844; m) J. C. Frias, G. Bobba, M. J. Cann, C. J. Hutchison, D. Parker, *Org. Biomol. Chem.* **2003**, *1*, 905–907; n) K. J. Franz, M. Nitz, B. Imperiali, *ChemBioChem* **2003**, *4*, 265–271; o) J. P. Cross, M. Lauz, P. D. Badger, S. Petoud, *J. Am. Chem. Soc.* **2004**, *126*, 16278–16279.
- [24] D. Parker, R. S. Dickins, H. Puschmann, C. Crossland, J. A. K. Howard, *Chem. Rev.* **2002**, *102*, 1977–2010.
- [25] O. Viratelle, J. P. Tenu, J. Garnier, J. Yon, *Biochem. Biophys. Res. Commun.* **1969**, *37*, 1036–1041.
- [26] a) Y. Urano, M. Kamiya, K. Kanda, T. Ueno, K. Hirose, T. Nagano, *J. Am. Chem. Soc.* **2005**, *127*, 4888–4894; b) J. Hofmann, M. Sernetz, *Anal. Biochem.* **1983**, *131*, 180–186.
- [27] J. P. Tenu, O. M. Viratelle, J. Garnier, J. Yon, *Eur. J. Biochem.* **1971**, *20*, 363–370.
- [28] W. H. Helhuish, *J. Phys. Chem.* **1961**, *65*, 229–235.
- [29] a) A. Beeby, I. M. Clarkson, R. S. Dickins, S. Faulkner, D. Parker, L. Royle, A. S. de Sousa, J. A. G. Williams, M. Woods, *J. Chem. Soc. Perkin Trans. 2* **1999**, 493–503; b) S. Quici, G. Marzanni, M. Cavazzini, P. L. Anelli, M. Botta, E. Gianolio, G. Accorsi, N. Armaroli, F. Barigelletti, *Inorg. Chem.* **2002**, *41*, 2777–2784.
- [30] M. Li, P. R. Selvin, *J. Am. Chem. Soc.* **1995**, *117*, 8132–8138.
- [31] A. V. Fowler, I. Zabin, *J. Biol. Chem.* **1978**, *253*, 5521–5525.
- [32] Q. Y. Chen, C. J. Feng, Q. H. Luo, C. Y. Duan, X. S. Yu, D. J. Liu, *Eur. J. Inorg. Chem.* **2001**, 1063–1069.
- [33] Y. M. Wang, Y. J. Wang, Y. L. Wu, *Polyhedron* **1999**, *18*, 109–117.

Received: May 24, 2007

Published online: November 8, 2007

Selective photoinactivation of protein function through environment-sensitive switching of singlet oxygen generation by photosensitizer

Takatoshi Yogo*[†], Yasuteru Urano*[‡], Akiko Mizushima[§], Hisato Sunahara*[†], Takanari Inoue*, Kenzo Hirose[¶], Masamitsu Iino[§], Kazuya Kikuchi^{||}, and Tetsuo Nagano*^{†**}

*Graduate School of Pharmaceutical Sciences and [§]Department of Pharmacology, Graduate School of Medicine, University of Tokyo, 7-3-1 Hongo, Bunkyo-ku, Tokyo 113-0033, Japan; [†]Core Research for Evolutional Science and Technology (CREST) and [‡]Precursory Research for Embryonic Science and Technology (PRESTO), Japan Science and Technology Agency, 4-1-8 Honcho Kawaguchi, Saitama 332-0012, Japan; [¶]Department of Cell Physiology, Nagoya University Graduate School of Medicine, 65 Tsurumai, Showa, Nagoya, Aichi 466-8550, Japan; and ^{||}Graduate School of Engineering, Division of Advanced Science and Biotechnology, Osaka University, 2-1 Yamada-oka, Suita, Osaka 565-0871, Japan

Edited by Koji Nakanishi, Columbia University, New York, NY, and accepted by the Editorial Board November 5, 2007 (received for review December 30, 2006)

Chromophore-assisted light inactivation is a promising technique to inactivate selected proteins with high spatial and temporal resolution in living cells, but its use has been limited because of the lack of a methodology to prevent nonspecific photodamage in the cell owing to reactive oxygen species generated by the photosensitizer. Here we present a design strategy for photosensitizers with an environment-sensitive off/on switch for singlet oxygen (¹O₂) generation, which is switched on by binding to the target, to improve the specificity of protein photoinactivation. ¹O₂ generation in the unbound state is quenched by photoinduced electron transfer, whereas ¹O₂ generation can occur in the hydrophobic environment provided by the target protein, after specific binding. Inositol 1,4,5-trisphosphate receptor, which has been suggested to have a hydrophobic pocket around the ligand binding site, was specifically inactivated by an environment-sensitive photosensitizer-conjugated inositol 1,4,5-trisphosphate receptor ligand without ¹O₂ generation in the cytosol of the target cells, despite light illumination, demonstrating the potential of environment-sensitive photosensitizers to allow high-resolution control of generation of reactive oxygen species in the cell.

activatable photosensitizer | boron dipyrromethene derivative | electron transfer | inositol 1,4,5-trisphosphate receptor

Chromophore-assisted light inactivation (CALI)(1) is a technique with great potential to inactivate proteins with high spatial and temporal resolution by using an antibody to direct a suitable fluorophore specifically to the protein of interest. Illumination induces local generation of reactive oxygen species (ROS), which react chemically with the adjacent antigen and inactivate it. Although CALI is a powerful technique, its use has been limited by the complexity of the procedures (i.e., the need to deliver a labeled antibody into cells or to use a laser as the light source). Several groups have reported alternative approaches. Genetically targeted CALI is one such method, in which the target protein is tagged with a tetracysteine tag that is recognized by a membrane-permeant biarsenical chromophore (FlAsH) (2, 3), or tagged with GFP (4–6). However, these methods also cause nonspecific damage, owing to the nonspecific binding of the biarsenical chromophore to cysteine-rich proteins (3, 7) in FlAsH-mediated photoinactivation, or to the use of a relatively high-power laser in EGFP-mediated CALI (4, 5). Current implementations of the CALI technique leave much to be desired, and highly specific inactivation of a protein of interest would require a methodology to control ROS generation by the photosensitizer in the cells with high spatial resolution.

We present here an approach for designing photosensitizers with an environment-controlled off/on switch for singlet oxygen (¹O₂) generation to improve the specificity of CALI. We have developed environment-sensitive photosensitizers (ESPer), which are acti-

ated by recognition of the hydrophobic (low-polarity) environment of the target protein, i.e., recognition of the appropriate environment switches on local generation of ¹O₂, whereas ¹O₂ is not generated in the polar cytosolic environment (Fig. 1*a*). The value of ESPer to control tightly the specificity of protein photoinactivation in the CALI technique was demonstrated by applying one of our ESPer for highly specific inactivation of inositol 1,4,5-trisphosphate receptor (IP₃R).

Results

Photoinduced Electron Transfer as a Mechanism to Control Photosensitization. We previously developed small molecule-based CALI for IP₃R by using a conventional photosensitizer (malachite green), and the physiological function of IP₃R was analyzed (8, 9). However, it would be advantageous for further biological applications if an activatable photosensitizer, which generates ROS only when it binds to IP₃R, could be developed. With this in mind, we focused on hydrophobic environment as a putative on-switch for an activatable photosensitizer. Intracellular proteins (e.g., the receptor of interest) usually consist of both hydrophobic and hydrophilic domains, and we considered that a hydrophobic photosensitizer moiety, if it is conjugated to a specific ligand of the target protein by a suitable linker, could be delivered to a hydrophobic domain near the ligand binding site inside the target protein by hydrophobic interaction. In the case of IP₃R, it has been suggested that IP₃R has a hydrophobic pocket around the binding site, based on the finding that IP₃ derivatives bearing a hydrophobic moiety have high binding affinity (10, 11). Thus, photosensitizers that could generate ROS only when they are activated by recognition of the hydrophobic environment around IP₃R should cause little or no nonspecific damage in the cytosol, where the environment is polar (Fig. 1*a*). To realize this concept, we selected photoinduced electron transfer (PeT) as a switch mechanism to control the ¹O₂ generation of photosensitizers. PeT is a well known mechanism through which the fluorescence of a fluorophore is quenched by electron transfer from the PeT donor to the lowest singlet-excited fluorophore (12, 13). Photosensitization is well known to

Author contributions: Y.U., T.Y., and T.N. designed research; T.Y. performed research; A.M., H.S., T.I., K.H., M.I., and K.K. contributed new reagents/analytic tools; and T.Y., Y.U., and T.N. wrote the paper.

The authors declare no conflict of interest.

This article is a PNAS Direct Submission. K.N. is a guest editor invited by the Editorial Board.

**To whom correspondence should be sent at the * address. E-mail: tlong@mol.f.u-tokyo.ac.jp.

This article contains supporting information online at www.pnas.org/cgi/content/full/0611717105/DC1.

© 2008 by The National Academy of Sciences of the USA

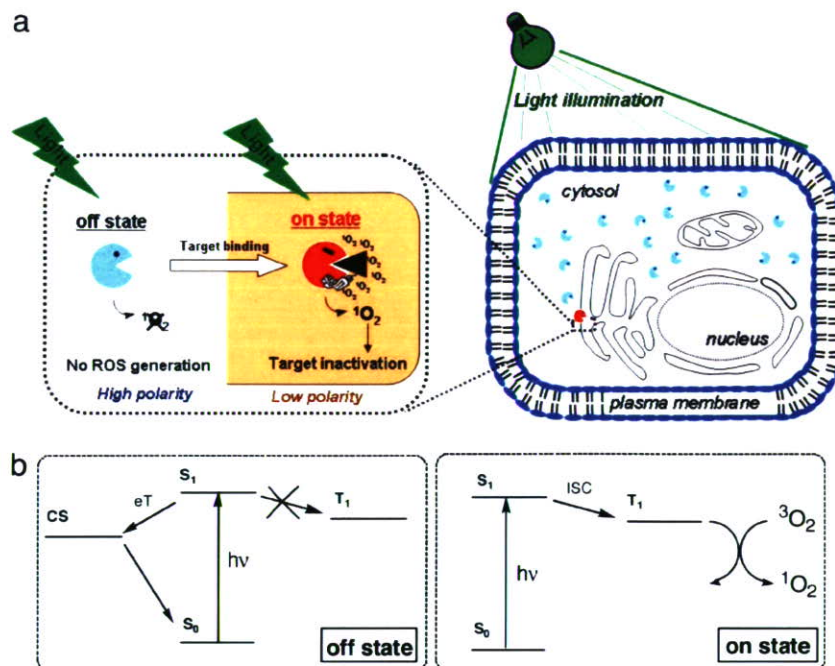


Fig. 1. Photoinduced electron transfer as a mechanism for controlling photosensitization in biological systems. (a) Schematic representation of protein photoinactivation by using ESPers. In the cytosolic polar environment, ESPers are in the off state of photosensitization (indicated by light blue) and do not generate 1O_2 . In the hydrophobic environment of the target, ESPers are in the on state of photosensitization (indicated by red) and generate 1O_2 , inducing inactivation of the nearby protein of interest. (b) Energy diagram of the ESPers. ISC, intersystem crossing; CS, charge separation; eT, electron transfer; S_0 , singlet ground state; S_1 , lowest singlet excited state; T_1 , lowest triplet excited state.

proceed also via the lowest singlet excited state (S_1), so it seemed reasonable that the photosensitization process could be controlled by PeT (Fig. 1b). Indeed, our preliminary results showed that 1O_2 generation of erythrosin derivatives upon light illumination was efficiently quenched by introducing electron-donating substituents into the benzene moiety (S. Kamakura, Y.U., and T.N., unpublished results). The PeT process is known to depend on the highest occupied molecular orbital (HOMO) energy level of the electron donor and the solvent polarity, so we designed and synthesized a series of photosensitizer derivatives by attaching an electron donor moiety to a photosensitizing chromophore for the specific inactivation of IP_3R in a hydrophobic environment.

Design and Synthesis of a Library of Candidate ESPers. We recently reported development of 4,4-difluoro-2,6-diiodo-1,3,5,7-tetramethyl-4-bora-3a,4a-diaza-s-indacene (2I-BDP) as a photosensitizer that generates 1O_2 uniformly in various solvents ranging from H_2O to *n*-hexane (14). We hypothesized that introduction of a suitable electron-donor moiety into 2I-BDP would allow the photosensitizing ability to be controlled precisely by means of PeT. To test this principle, we synthesized various 2I-BDP derivatives bearing a substituted benzene moiety (1a–1f), in which the use of various substituents (methyl, methoxy, or amino) as electron donors was expected to allow the HOMO energy level to be finely tuned (Fig. 2a). These 2I-BDP derivatives have high values of extinction coefficient ($\epsilon \approx 1 \times 10^5 \text{ M}^{-1}\text{cm}^{-1}$) at $\approx 530 \text{ nm}$ [supporting information (SI) Fig. 5]. We then examined the ability of these 2I-BDP derivatives to generate 1O_2 in various solvents, from polar to nonpolar, by observing the disappearance of 1,3-diphenylisobenzofuran (DPBF), which is known to react with 1O_2 under light illumination (15) (for detailed experimental procedures, see SI Materials and Methods). The relative efficiencies of 1O_2 generation (ϕ_Δ) of 1a–1f in each solvent are summarized in Fig. 2b. These 2I-BDP deriva-

tives had almost identical absorbance maximum wavelengths (SI Fig. 5), but the ϕ_Δ of certain 2I-BDP derivatives, i.e., those having an electron donor moiety with high HOMO energy (1c–1f), was significantly quenched in polar solvents such as CH_3CN and $MeOH$, compared with that of 1a and 1b, whose benzene moiety has a relatively low HOMO energy. These results suggested that ϕ_Δ of these 2I-BDP derivatives could indeed be controlled by PeT. We then examined the effect of solvent polarity. We have recently developed environment-sensitive fluorescence probes based on the boron dipyrromethene (BODIPY) fluorophore, whose fluorescence properties were shown to be controlled by PeT and by solvent effects on the PeT (see also SI Fig. 6). Because 2I-BDP derivatives are iodinated derivatives of BODIPY, they may behave similarly. Fig. 2b shows that ϕ_Δ of 1c–1f was dependent on the solvent polarity (i.e., dielectric constant, DC). Compounds 1c–1e were unable to generate 1O_2 (i.e., they were in the off state of photosensitization) in solvents more polar than acetone (DC ≈ 20.7), whereas the 1O_2 -generating ability was restored (i.e., the compounds were in the on state of photosensitization) in solvents less polar than CH_2Cl_2 (DC ≈ 9.14). On the other hand, 1f was still in the off state in CH_2Cl_2 , and was switched on only in solvents less polar than $CHCl_3$ (DC ≈ 4.81), indicating that the threshold for off–on switching of 1O_2 generation is dependent on the HOMO energy level of the benzene moiety. These results indicated that appropriately designed 2I-BDP derivatives, having a HOMO energy around -0.17 to -0.19 hartree, could be used as environment-sensitive photosensitizers (ESPers), which would be activated by recognizing a hydrophobic environment, and would generate 1O_2 in such an environment, but not in a polar environment. We then examined whether ESPers could be activated by recognizing a hydrophobic environment at the cellular level.

Design of ESPer-Conjugated IP_3 Ligand for Specific Photoinactivation of IP_3R . We next designed and synthesized an ESPer-conjugated IP_3R ligand for photoinactivation of IP_3R and examined whether

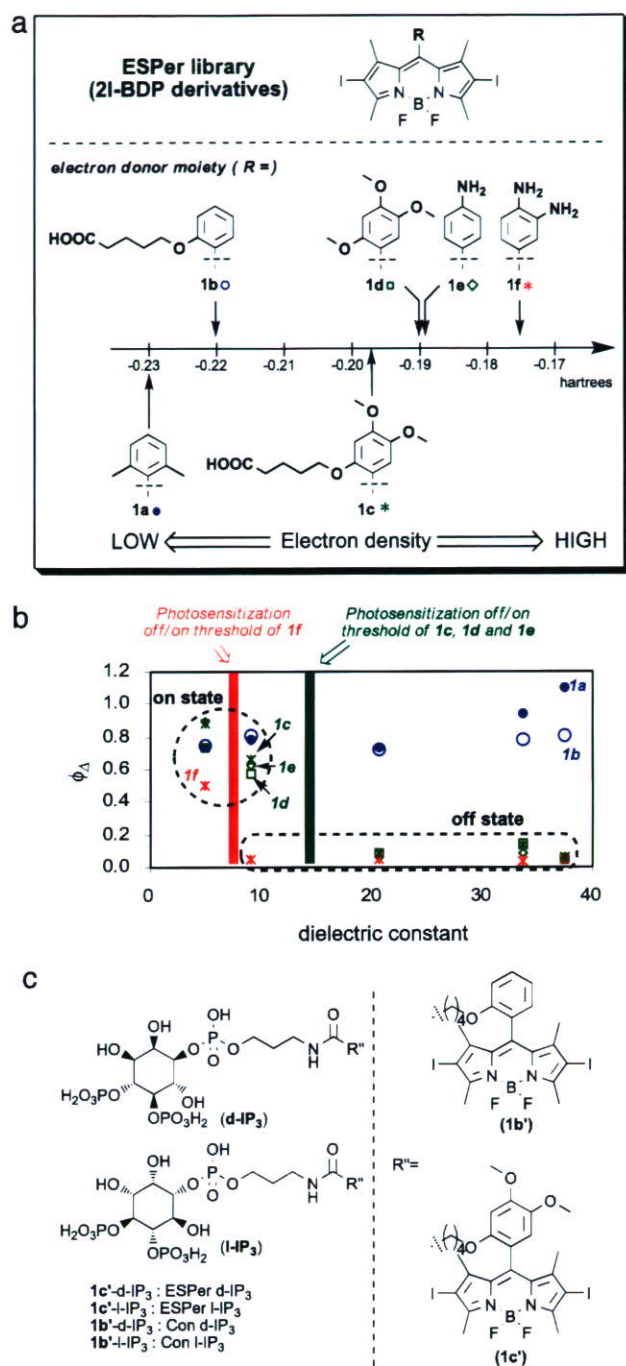


Fig. 2. Development of a library of ESPers making use of the solvent effect on PeT. (a) Structures of 2I-BDP derivatives with various benzene moieties. (b) Relationship between the relative efficiency of $^1\text{O}_2$ generation (ϕ_{Δ}) of 2I-BDP derivatives (1a–1f) and the dielectric constant of the solvent. Solvents used in this study were CH_3CN , MeOH, acetone, CH_2Cl_2 , and CHCl_3 , whose dielectric constants are 37.5, 33.6, 20.7, 9.14, and 4.81, respectively. Filled blue circle, 1a; open blue circle, 1b; green star, 1c; open green square, 1d; open green diamond, 1e; red star, 1f. (c) Structures of ESPer 1c-conjugated IP₃ derivatives and control (Con) photosensitizer 1b-conjugated IP₃ derivatives; d- and l- refer to the d and l absolute configurations of inositol 1,4,5-trisphosphate.

it could generate $^1\text{O}_2$ specifically in the vicinity of IP₃R. IP₃R has been suggested to have a hydrophobic pocket around the binding site, which was estimated to be similar in polarity to CH_2Cl_2

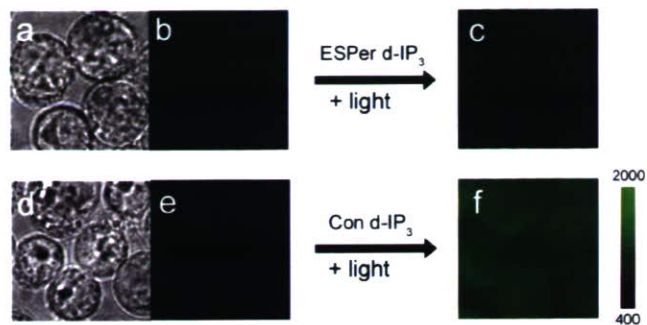


Fig. 3. Imaging of photosensitizer-induced nonspecific cytosolic $^1\text{O}_2$ generation in the presence of ESPer d-IP₃, compared with that in the presence of Con d-IP₃, using a fluorescence probe for $^1\text{O}_2$ (DMAX-2). Permeabilized DT40 cells (wild type) were loaded with 3 μM ESPer d-IP₃ or Con d-IP₃ and 10 μM DMAX-2, followed by illumination with green light (BP530–550 nm, 1.5 mW/cm^2 , 20 sec). Fluorescence images of DMAX-2 were acquired with a fluorescence microscope by excitation with blue light (BA470–490) before and after green light illumination. (a–c) Single DT40 cells under transmitted light (a) and fluorescence image excited with blue light before (b) and after (c) excitation of ESPer d-IP₃ with green light. (d–f) Single DT40 cells under transmitted light (d) and fluorescence image excited with blue light before (e) and after (f) excitation of Con d-IP₃ with green light. Color scale on the right is the relative fluorescence intensity. (Scale bar, 10 μm .)

(DC \approx 9.14) by the use of environment-sensitive fluorescence probes (SI Materials and Methods and SI Fig. 6). Thus, we considered that 1c and 1d (Fig. 2a), which have a trimethoxybenzene moiety, might be suitable ESPers to recognize the environment around IP₃R. We synthesized an IP₃ derivative bearing 1c (Fig. 2c). As a control (Con) compound, we also synthesized an IP₃ derivative bearing 1b, whose off/on switch for $^1\text{O}_2$ generation is constitutively on (Fig. 2a and b), regardless of the environment. d-IP₃ derivatives were designed as IP₃ ligands that bind to IP₃R, and l-IP₃ derivatives (optical isomers of d-IP₃), which are expected to have the same photochemical properties as those of d-IP₃ derivatives, although with much weaker agonistic effects on IP₃R (8), were also synthesized (Fig. 2c). These photosensitizer-conjugated d-IP₃ derivatives induced Ca^{2+} release via IP₃R in a dose-response manner with an EC_{50} of 3 μM for both ESPer d-IP₃ and Con d-IP₃, whereas the photosensitizer-conjugated l-IP₃ derivatives had almost no Ca^{2+} release activity (SI Fig. 7).

Imaging of Photosensitizer-Induced Nonspecific Damage Caused by ESPer d-IP₃ and Con d-IP₃ in the Cytosolic Polar Environment. We examined whether ESPer d-IP₃ outside the hydrophobic IP₃R environment (e.g., in the cytosolic polar environment) indeed lacked $^1\text{O}_2$ -generating ability (off state of photosensitization) despite light illumination, whether $^1\text{O}_2$ -generating ability was recovered in the vicinity of IP₃R (on state of photosensitization), and whether IP₃R could be inactivated by the $^1\text{O}_2$ generated (as illustrated in Fig. 1a). We first studied whether ESPer d-IP₃ generated $^1\text{O}_2$ in the cytosol in the cells by fluorescence imaging of $^1\text{O}_2$ generation with a fluorescent probe for $^1\text{O}_2$ (DMAX-2) (16) in permeabilized DT40 cells (wild type). Permeabilized DT40 cells were loaded with 3 μM ESPer d-IP₃ (or Con d-IP₃) and 10 μM DMAX-2, followed by illumination with green light (BP530–550 nm, 1.5 mW/cm^2 , 20 sec) to excite the photosensitizer. ESPer d-IP₃-loaded cells showed little, if any, fluorescence increase of DMAX-2 upon light illumination (Fig. 3 a–c). On the other hand, Con d-IP₃-loaded cells showed a marked fluorescence increase of DMAX-2 in cytosol (Fig. 3 d–e), owing to nonspecific $^1\text{O}_2$ generation in the polar cytosolic environment, as shown in Fig. 2b. The fluorescence increase induced by DMAX-2 in Con d-IP₃-loaded cells was inhibited by adding a $^1\text{O}_2$ quencher

(20 mM NaN₃) (SI Fig. 8). These results clearly demonstrate that nonspecific photosensitizer-induced ¹O₂ generation outside the environment of interest can be significantly reduced by designing a suitable photosensitizer with an off/on switch for ¹O₂ generation. We next investigated whether ESPer-IP₃ could specifically acquire ¹O₂-generating ability in the hydrophobic environment in the vicinity of IP₃R.

ESPer-Mediated Photoinactivation of IP₃R in Cells. We examined whether ESPer d-IP₃, which has been shown not to generate ¹O₂ in cytosol (Fig. 3), could induce IP₃R inactivation through ¹O₂ generation after recognition of the hydrophobic environment of IP₃R in DT40 cells (wild type). DT40 cells were loaded with FuraFura acetoxymethyl ester (AM) as a Ca²⁺ indicator, then permeabilized with β-escin to retain the probe only in the endoplasmic reticulum (ER), enabling us to continuously monitor luminal Ca²⁺ concentration ([Ca²⁺]_l) within the store (17). An increase in [Ca²⁺]_l was observed upon activation of sarco/endoplasmic reticulum Ca²⁺-ATPase (SERCA) with application of both Ca²⁺ and MgATP, followed by a decrease upon addition of IP₃. First, by monitoring [Ca²⁺]_l within permeabilized DT40 cells, we measured the IP₃-induced Ca²⁺ release (IICR) rate at 10 μM IP₃. The cells were then illuminated for 5 sec with green light (535 ± 25 nm, 20 mW) in the presence of 2 μM test photosensitizer. The photosensitizer was washed out, and the IICR rate was measured again and compared with that at pretreatment. A considerable decrease in the IICR rate was observed (IICR rate pretreatment = 0.194 ± 0.0084 sec⁻¹, IICR rate after treatment = 0.093 ± 0.0071 sec⁻¹; Fig. 4*a* and *b*) after light illumination in the presence of ESPer d-IP₃. The extent of this decrease of the IICR rate owing to ESPer d-IP₃-mediated photoinactivation of IP₃R was similar to that in the case of Con d-IP₃-mediated photoinactivation (Fig. 4*b*). On the other hand, the optical isomers (i.e., ESPer l-IP₃ and Con l-IP₃) did not cause receptor inactivation upon light illumination (Fig. 4*a* and *b*), indicating that the inactivation of IP₃R required the binding of ESPer d-IP₃ to the receptor. Furthermore, the photoinactivation caused by ESPer d-IP₃ or Con d-IP₃ was inhibited by adding a ¹O₂ quencher (20 mM NaN₃) to the intracellular solution (Fig. 4*b*), suggesting that the inactivation of IP₃R by ESPer d-IP₃ was mediated by ¹O₂. The activity of SERCA protein, which is colocalized with IP₃R on the ER membrane (18), was not affected by ESPer d-IP₃-mediated photoinactivation (SI Fig. 9), suggesting that little or no nonspecific damage to nontargeted protein present on the same intracellular organelle as IP₃R was induced by light illumination. These results demonstrated that ESPer d-IP₃ could bind to IP₃R, where it recognized the hydrophobic environment, and was activated to generate ¹O₂, resulting in highly specific receptor inactivation.

Discussion

We have developed an environment-sensitive photosensitizer, which is activated upon recognizing the hydrophobic environment of a protein of interest and generates ¹O₂ only within this environment to achieve highly specific photoinactivation based on the CALI technique. We designed an ESPer-conjugated IP₃R ligand (ESPer d-IP₃), which would be activated in the range of polarity of CH₂Cl₂ (Fig. 2). ESPer d-IP₃ did not generate ¹O₂ outside the IP₃R environment even under light illumination (Fig. 3), but acquired ¹O₂-generating ability in the hydrophobic environment in the vicinity of IP₃R (Fig. 4). We now plan to apply ESPer d-IP₃ to neuronal cells to examine the specificity of ESPer d-IP₃ in intact cells and study physiological functions of IP₃R. Such an activatable photosensitizer permits highly regiospecific generation of ¹O₂ at the target protein, with little or no nonspecific phototoxicity elsewhere in the cell. So far, the use of photosensitizers has required great care to avoid nonspecific damage, and the specificity of the photosensitizing effect has

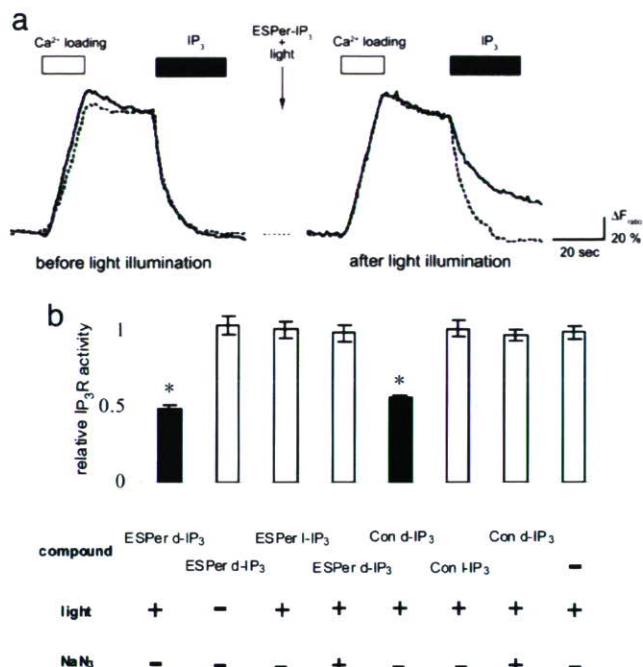


Fig. 4. ESPer-mediated light inactivation of the target protein in a hydrophobic environment. (a) ESPer d-IP₃-mediated light inactivation of IP₃R. After measurement of the IICR rate at 10 μM IP₃, permeabilized DT40 cells (wild type) were pretreated with 2 μM ESPer d-IP₃ (solid line) or 2 μM ESPer l-IP₃ (dotted line) followed by light illumination at 530 nm (20 mW/cm²) for 5 sec. After the irradiation and immediate washout of the ESPer d- or l-IP₃-containing solution, the IICR rate at 10 μM IP₃ of the illuminated cells was measured. Traces show Ca²⁺ responses in a single DT40 cell. Note that there is a considerable difference between the IICR rates before and after the treatment. (b) The IICR rate after 5-sec light illumination with or without test compound, light illumination, and 20 mM NaN₃ was normalized to that before illumination. A significant difference was found when the relative Ca²⁺ release rate of the illuminated cells loaded with ESPer d-IP₃ or Con d-IP₃ in the absence of NaN₃ (filled columns) was compared with that of cells under other conditions (open columns) [$P < 0.0001$, Fisher's probable least-squares difference (PLSD) test]. The number of images of analyzed cells was 25, acquired in three independent experiments. Error bars represent SEM.

often been dependent on the precise localization of photosensitizers in the cell or whole body (19), which cannot be easily predicted and requires much experimental effort to determine. On the other hand, our design approach to ESPers enables us to predict the efficiency of ¹O₂ generation by calculation of the HOMO energy level of the electron donor moiety, and we could prepare a series of photosensitizers with off/on switches operating at various cellular properties, such as pH and specific enzyme. Furthermore, ESPers could be excited by using conventional equipment such as the xenon light of a fluorescence microscope. Of course, when designing a novel activatable photosensitizer for the inactivation of another target protein based on the above-mentioned approach, specificity should be thoroughly examined; however, our rational design strategy should expand the applicability of photosensitizers in biological research, as well as clinical applications, by allowing tight control of the regiospecificity of photosensitization through switching on ¹O₂-generating ability only after binding of the photosensitizer to the designated target.

Materials and Methods

Chemical Synthesis. For detailed synthetic procedures, characterization of products, and photochemical properties of BODIPY derivatives, see *SI Materials and Methods* and *SI Schemes 1–5*.

Fluorescence Imaging. Fluorescence images were acquired with an inverted microscope (IX71; Olympus), equipped with a cooled CCD camera (Cool Snap HQ; Roper Scientific) and a xenon lamp (AH2-RX; Olympus). The whole system was controlled with MetaFluor 6.1 software (Universal Imaging). For imaging $^1\text{O}_2$ generation by DMAX-2 (for details of the characteristics of DMAX-2, see also SI Fig. 10), DT40 cells (wild type) attached to the coverslips were permeabilized with $60\ \mu\text{M}$ β -escin for 1–2 min. Cells were loaded with $3\ \mu\text{M}$ Con d-IP₃ or ESPer d-IP₃ and $10\ \mu\text{M}$ DMAX-2, and fluorescence images (excitation filter, BA470–490; dichroic mirror, DM505; emission filter, BA510–550; Olympus) were acquired immediately after illumination with green light (BP530–550 nm, $1.5\ \text{mW}/\text{cm}^2$, 20 sec).

Luminal Ca^{2+} Imaging of DT40 Cells. Ca^{2+} imaging of DT40 cells was performed as described previously (17) (see also SI Materials and Methods). Briefly, DT40 cells (wild type) were loaded with Fura2/AM, a membrane-permeant, low-affinity Ca^{2+} indicator, which enters both the cytosol and organelles. Fura2/AM-loaded cells were then permeabilized with β -escin so that Fura2/AM was retained only in the ER, enabling us to continuously monitor luminal Ca^{2+} concentration ($[\text{Ca}^{2+}]$) within the store. An increase in $[\text{Ca}^{2+}]$ was observed

upon activation of sarco/endoplasmic reticulum Ca^{2+} -ATPase (SERCA) with application of both Ca^{2+} and MgATP, followed by a decrease upon addition of IP₃. This Ca^{2+} loading and release procedure can be repeated reproducibly in the same cells, and the rate constant of IP₃-induced Ca^{2+} release (IICR) was used as an index of IP₃R activity.

Light Illumination for Photoinactivation of IP₃R. First, by monitoring $[\text{Ca}^{2+}]$ within permeabilized DT40 cells, we measured the IICR rate at $10\ \mu\text{M}$ IP₃. The cells were then illuminated for 5 sec in the presence of $2\ \mu\text{M}$ test photosensitizer with a xenon lamp (AH2-RX), which was filtered to $\approx 535 \pm 25\ \text{nm}$ by an excitation filter (HQ535/50; Chroma Technology) through the objective lens under the fluorescence microscope. The photosensitizer was washed out, and the IICR rate was measured again and compared with the pretreatment value.

ACKNOWLEDGMENTS. This study was supported by a grant for Precursory Research for Embryonic Sciences and Technology from the Japan Science and Technology Agency, Research Grants 16651106 and 16689002 from the Ministry of Education, Culture, Sports, Science and Technology of the Japanese Government, and a grant from the Kato Memorial Bioscience Foundation to Y.U.

- Jay D-G (1988) *Proc Natl Acad Sci USA* 85:5454–5458.
- Marek K-W, Davis G-W (2002) *Neuron* 36:805–813.
- Tour O, Meijer R-M, Zacharias D-A, Adams S-R, Tsien R-Y (2003) *Nat Biotechnol* 21:1505–1508.
- Rajfur Z, Roy P, Otey C, Romer L, Jacobson K (2002) *Nat Cell Biol* 4:286–293.
- Tanabe T, Oyama M, Fujita K, Dai P, Tanaka H, Takamatsu T (2005) *Nat Methods* 2:503–505.
- Bulina M-E, Chudakov D-M, Britanova O-V, Yanushevich Y-G, Staroverov D-B, Chepurnykh T-V, Merzlyak E-M, Shkrob M-A, Lukyanov S, Lukyanov, K-A (2006) *Nat Biotechnol* 24:95–99.
- Stroffekova K, Proenza C, Beam K-G (2001) *Pflügers Arch* 442:859–866.
- Inoue T, Kikuchi K, Hirose K, Iino M, Nagano T (2003) *Chem Biol* 10:503–509.
- Yogo T, Kikuchi K, Inoue T, Hirose K, Iino M, Nagano T (2004) *Chem Biol* 11:1053–1058.
- Inoue T, Kikuchi K, Hirose K, Iino M, Nagano T (1999) *Bioorg Med Chem Lett* 9:1697–1702.
- Nakanishi W, Kikuchi K, Inoue T, Hirose K, Iino M, Nagano T (2002) *Bioorg Med Chem Lett* 12:911–913.
- Miura T, Urano Y, Tanaka K, Nagano T, Ohkubo K, Fukuzumi S (2003) *J Am Chem Soc* 125: 8666–8671.
- Urano Y, Kamiya M, Kanda K, Ueno T, Hirose K, Nagano T (2005) *J Am Chem Soc* 127:4888–4894.
- Yogo T, Urano Y, Ishitsuka Y, Maniwa F, Nagano T (2005) *J Am Chem Soc* 127:12162–12163.
- Lissi E-A, Encinas M-V, Lemp E, Rubio M-A (1993) *Chem Rev* 93:699–723.
- Tanaka K, Miura T, Umezawa N, Urano Y, Kikuchi K, Higuchi T, Nagano T (2001) *J Am Chem Soc* 123:2530–2536.
- Miyakawa T, Maeda A, Yamazawa T, Hirose K, Kurosaki T, Iino M (1999) *EMBO J* 18:1303–1308.
- Hirose K, Iino M (1994) *Nature* 372:791–794.
- Jari G (1996) *J Photochem Photobiol B* 36:87–93.

Insights into Zn²⁺ homeostasis in neurons from experimental and modeling studies

Robert A. Colvin, Ashley I. Bush, Irene Volitakis, Charles P. Fontaine, Dustin Thomas, Kazuya Kikuchi and William R. Holmes

Am J Physiol Cell Physiol 294:726-742, 2008. First published Jan 9, 2008;
doi:10.1152/ajpcell.00541.2007

You might find this additional information useful...

This article cites 61 articles, 29 of which you can access free at:

<http://ajpcell.physiology.org/cgi/content/full/294/3/C726#BIBL>

Updated information and services including high-resolution figures, can be found at:

<http://ajpcell.physiology.org/cgi/content/full/294/3/C726>

Additional material and information about *AJP - Cell Physiology* can be found at:

<http://www.the-aps.org/publications/ajpcell>

This information is current as of March 17, 2008 .

Insights into Zn²⁺ homeostasis in neurons from experimental and modeling studies

Robert A. Colvin,^{1,2} Ashley I. Bush,^{5,6} Irene Volitakis,^{5,6} Charles P. Fontaine,¹ Dustin Thomas,¹ Kazuya Kikuchi,⁴ and William R. Holmes^{1,2,3}

¹Department of Biological Sciences, ²Neuroscience Program, and ³Quantitative Biology Institute, Ohio University, Athens, Ohio; ⁴Graduate School of Engineering, Department of Materials and Life Sciences, Osaka University, Osaka, Japan; and ⁵The Mental Health Research Institute of Victoria and ⁶Department of Pathology, The University of Melbourne, Parkville, Victoria, Australia

Submitted 14 November 2007; accepted in final form 29 December 2007

Colvin RA, Bush AI, Volitakis I, Fontaine CP, Thomas D, Kikuchi K, Holmes WR. Insights into Zn²⁺ homeostasis in neurons from experimental and modeling studies. *Am J Physiol Cell Physiol* 294: C726–C742, 2008. First published January 9, 2008; doi:10.1152/ajpcell.00541.2007.—To understand the mechanisms of neuronal Zn²⁺ homeostasis better, experimental data obtained from cultured cortical neurons were used to inform a series of increasingly complex computational models. Total metals (inductively coupled plasma-mass spectrometry), resting metallothionein, ⁶⁵Zn²⁺ uptake and release, and intracellular free Zn²⁺ levels using ZnAF-2F were determined before and after neurons were exposed to increased Zn²⁺, either with or without the addition of a Zn²⁺ ionophore (pyrithione) or metal chelators [EDTA, clioquinol (CQ), and *N,N,N',N'*-tetrakis(2-pyridylmethyl)ethylenediamine]. Three models were tested for the ability to match intracellular free Zn²⁺ transients and total Zn²⁺ content observed under these conditions. Only a model that incorporated a muffler with high affinity for Zn²⁺, trafficking Zn²⁺ to intracellular storage sites, was able to reproduce the experimental results, both qualitatively and quantitatively. This “muffler model” estimated the resting intracellular free Zn²⁺ concentration to be 1.07 nM. If metallothionein were to function as the exclusive cytosolic Zn²⁺ muffler, the muffler model predicts that the cellular concentration required to match experimental data is greater than the measured resting concentration of metallothionein. Thus Zn²⁺ buffering in resting cultured neurons requires additional high-affinity cytosolic metal binding moieties. Added CQ, as low as 1 μM, was shown to selectively increase Zn²⁺ influx. Simulations reproduced these data by modeling CQ as an ionophore. We conclude that maintenance of neuronal Zn²⁺ homeostasis, when challenged with Zn²⁺ loads, relies heavily on the function of a high-affinity muffler, the characteristics of which can be effectively studied with computational models.

muffler; zinc buffering; computational model; metal ion transport and homeostasis; metallothionein

NUMEROUS EXAMPLES OF COMPUTATIONAL models of cellular Ca²⁺ homeostasis exist; however, the same level of effort has not been directed toward metal homeostasis, in particular Zn²⁺. This is surprising in light of the fact that dysregulation of neuronal Zn²⁺ homeostasis is recognized as a contributing factor to Alzheimer's disease pathology and selective neuronal death after brain ischemia (21). The paucity of modeling studies is due, at least in part, to the lack, until very recently, of high-affinity Zn²⁺-selective fluorophores, which are able to monitor changes in free intracellular Zn²⁺ (note that free

intracellular Zn²⁺ is generally accepted to be as much as 1,000-fold less than Ca²⁺) (see Refs. 2, 3, 38). We now have a cadre of fluorophores available with good Zn²⁺ selectivity and sensitivity (59). Armed with such tools, recent studies of eukaryotic cellular mechanisms of Zn²⁺ homeostasis have clearly shown similarities with cellular Ca²⁺ homeostasis, although important differences do exist (for review, see Ref. 8). These studies have now provided the experimental data needed to inform computational models.

Like other cells studied (37, 38), we have shown that neurons maintain a large intracellular buffer capacity for Zn²⁺, such that even micromolar Zn²⁺ loads result in only small changes in free intracellular Zn²⁺ concentration (6, 10). The sources of cellular Zn²⁺ buffering might include cytosolic binding proteins [e.g., the thionein/metallothionein (MT) pair] (37), binding to small molecules such as glutathione (40), sequestration into cytoplasmic organelles (35, 53), and eventually efflux (34, 49). Intracellular free Zn²⁺ is thought to be in equilibrium with many soluble cytosolic Zn²⁺ binding proteins. The metallothionein/thionein (MT/T) pair is a well-studied example of such a protein (37). The apoprotein can bind a total of seven Zn²⁺ ions in two domains, coordinated by several cysteine ligands. Unfortunately, the binding and release kinetics of Zn²⁺ with MT/T are still poorly understood, which, in turn, limits our understanding of its role as a cytosolic Zn²⁺ buffer and/or chaperone. Studies of binding and release kinetics of the MT-2 isoform have suggested that the two domains differ significantly in Zn²⁺ affinity (33, 39).

Two different Zn²⁺ transporter gene families [solute-linked carrier (SLC) 39 and SLC30] have been identified; each family probably has a unique transport mechanism, function, and cellular location. Expression of SLC39 gene family members [protein name: Zrt/Irt-like protein (ZIP)] has been observed in most eukaryotic organisms (for review, see Ref. 24). However, the transport mechanism(s) of mammalian SLC39 proteins has been only partially solved (22, 23). These studies provide convincing evidence that the SLC39A1 protein is normally targeted to the plasma membrane and mediates Zn²⁺ influx, although other family members are targeted to the Golgi (30). The transporter appears to function by simple facilitated transport, dependent on a concentration gradient to provide the free energy for net movement of Zn²⁺ into the cell.

Address for reprint requests and other correspondence: R. A. Colvin, Dept. of Biological Sciences, Ohio Univ., Athens, OH, 45701 (e-mail: colvin@ohio.edu).

The costs of publication of this article were defrayed in part by the payment of page charges. The article must therefore be hereby marked “advertisement” in accordance with 18 U.S.C. Section 1734 solely to indicate this fact.

Like the SLC39 gene family, SLC30 gene [protein name: zinc transporter (ZnT)] family members are found at all phylogenetic levels in eukaryotic organisms (24). The function, tissue location, and mechanism(s) of Zn²⁺ transport by SLC30 gene family members are best studied for the mammalian protein ZnT-1 (SLC30A1 gene) and its several homologs (49), where it was shown to be localized to the plasma membrane and presumably transports Zn²⁺ out of the cell (34). Unfortunately, these studies and others have not delineated a clear mechanism of transport. Many SLC30 family member proteins are preferentially localized to intracellular membranes, where they have more limited, tissue-specific expression, probably related to physiological intracellular Zn²⁺ sequestration (for review, see Ref. 15). SLC30A3 is required for the sequestration of Zn²⁺ into synaptic vesicles of glutamatergic neurons (48). Several recent studies demonstrate the localization of SLC30A5-7 proteins to the secretory pathway (in particular, the Golgi and vesicular compartment) and their importance in Zn²⁺ homeostatic mechanisms (16, 55, 56). Recent studies demonstrate also that Zn²⁺ can enter the matrix of brain mitochondria by mitochondrial uniporter-dependent and -independent mechanisms (43).

The first step in understanding the roles that Zn²⁺ plays in various brain pathologies requires a precise description of the neuronal Zn²⁺ metallo and normal mechanisms of Zn²⁺ homeostasis. To accomplish this goal, we have developed a computational model of neuronal Zn²⁺ homeostasis, highly constrained by experimentally derived parameter values. The model faithfully reproduced acute changes in intracellular free Zn²⁺ concentration observed in cultured rat cortical neurons when Zn²⁺ influx was increased. Experimental data have suggested that clioquinol (CQ) (a Zn²⁺-selective metal chelator with therapeutic potential in Alzheimer's disease) has Zn²⁺ ionophoric actions at the plasma membrane (13). By incorporating CQ with ionophoric activity into the model, the model was able to match observed changes in free intracellular Zn²⁺ observed after CQ addition.

MATERIALS AND METHODS

Primary culture of embryonic cortical neurons. The care and use of animals in this study adhered to the American Physiological Society's *Guiding Principles in the Care and Use of Animals*. All experimental procedures were approved by the Ohio University Institutional Animal Care and Use Committee. Primary culture of embryonic (E-17-18) cortical neurons from Sprague-Dawley rats was performed as described previously (10). After 24 h, the plating media was replaced with fresh neurobasal (NB) media (Gibco BRL), supplemented with 0.5 mM glutamine and 2% B-27 (Gibco BRL). Media was subsequently changed as needed.

Fluorescence measurements from cortical neurons attached to glass coverslips. Pluronic acid (20% in DMSO) (Invitrogen) was mixed 1:1 (vol/vol) with 10 mM ZnAF-2F (diacetyl, cell-permeant form) (28), dissolved in DMSO (Sigma). The resulting mixture was diluted to 5 μM in Locke's buffer pH 7.4 (154 mM NaCl₂, 5.6 mM KCl, 2.3 mM CaCl₂, 1 mM MgCl₂, 5 mM HEPES, and 10 mM glucose). Glass coverslips with attached cortical neurons were incubated for 30 min at 37°C in a humid 5% CO₂ incubator with 5 μM ZnAF-2F. The coverslips were inserted into a coverslip holder, rinsed once with low-calcium (loCa) Locke's buffer, pH 8, for 1 min with gentle stirring. After rinsing, the coverslip holder and coverslip were moved to a new cuvette with fresh loCa Locke's buffer. Buffers were bubbled with O₂ (to remove dissolved CO₂) and then adjusted to pH

8, because these conditions give maximum Zn²⁺ uptake (6). To minimize effects of extracellular Ca²⁺ entering the neurons and possibly affecting intracellular ZnAF-2F fluorescence, extracellular Ca²⁺ was reduced to 0.5 mM. This concentration was chosen by adding ionomycin to cultured neurons in the presence of decreasing extracellular Ca²⁺ (without addition of Zn²⁺) until no observable effect on intracellular ZnAF-2F fluorescence was observed (data not shown). Continuous readings of cellular fluorescence intensity (counts per second using the FluoroMax-3 spectrofluorometer, Horiba Jobin Yvon) were obtained using excitation 492 nm and emission of 516 nm. Data presented as rate of fluorescence increase ($\Delta F/F_0$) were calculated as described previously (9). Experimentally obtained fluorescence intensity changes could be expressed as fractional saturation of ZnAF-2F by utilizing data obtained from the addition of pyrithione followed by *N,N,N',N'*-tetrakis(2-pyridylmethyl)ethylenediamine (TPEN) at the conclusion of an experiment. ZnAF-2F fluorescence after pyrithione was used as 100% saturation, and fluorescence after TPEN addition was used as 0% saturation.

Image capture and analysis. Cells were examined using conventional epifluorescence using an inverted microscope (Nikon, Diaphot 300) equipped with a Nikon PlanApo 60/1.40 oil differential interference contrast objective. The coverslips were placed in a sealed perfusion chamber (RC-30, Warner Instruments) that was held at a constant 37°C, and image capture and analysis were performed as described previously (41).

Inductively coupled plasma-mass spectrometry analysis and ⁶⁵Zn²⁺ uptake experiments. Cortical neurons after various treatments were washed three times with loCa Locke's buffer, pH 8, containing 100 μM EDTA and then moved to a new plate on ice, where they were aspirated dry and finally frozen at -70°C at least overnight. Later the plates were brought to room temperature, and, to each well, 225-μl Chelex (Sigma) washed 50 mM HEPES, pH 7.4, was added, and the coverslips were scraped clean to suspend the cellular debris. Total protein was determined by the Bio-Rad protein assay reagent using bovine serum albumin as a standard. The remaining cell suspension was desiccated in a centrifuge under vacuum at 60°C (Vacufuge, Eppendorf) for inductively coupled plasma-mass spectrometry (ICP-MS) analysis. Measurements were made using an UltraMass 700 (Varian), as described previously (61).

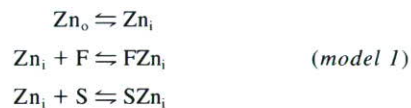
For ⁶⁵Zn²⁺ uptake, cortical neurons were treated identically, except that ⁶⁵Zn²⁺ (Brookhaven National Laboratory) was added. Depending on the experiment, ⁶⁵Zn²⁺ was mixed with non-radioactive Zn²⁺ to obtain a final specific activity between 0.001 and 0.005 μCi/μl. The specific activity of each reaction buffer was determined by assaying an aliquot for radioactivity. For calculation purposes, specific activity was expressed as counts per minute per nanomole Zn²⁺. ⁶⁵Zn²⁺ was determined in a liquid scintillation counter. Using the specific activity and protein, raw counts per minute were converted to nanomoles per milligram for each well and then could be compared directly to total Zn²⁺ content determined by ICP-MS.

Determination of intracellular ZnAF-2F concentration. Determination of intracellular fluorophore concentration usually involves loading cells, then lysing the cells to release fluorophore and comparing maximal fluorescence of the released fluorophore to a standard curve (e.g., Refs. 12, 38). We used a similar method; however, we found it was not necessary to lyse the cells. Neurons attached to coverslips were preloaded with 5 μM ZnAF-2F, washed, and then exposed to 5 μM pyrithione/30 μM Zn²⁺ [maximum fluorescence (F_{max})] followed by 200 μM TPEN [minimum fluorescence (F_{min})]. The resulting cellular F value ($F_{max} - F_{min}$) was compared with a calibration curve of ZnAF-2F fluorescence obtained in a cuvette using serial dilutions of ZnAF-2F at saturating Zn²⁺ concentrations with the same instrument settings and sensitivity as used for neurons attached to a coverslip. The intracellular concentration of ZnAF-2F obtained from the calibration curve only needed to be corrected for the actual

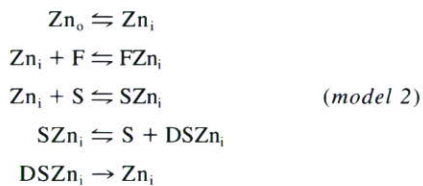
volume of the neurons attached to the coverslip illuminated by the excitation beam. The area of the coverslip illuminated by the excitation beam was determined by placing a white index card in the beam and marking its size on the card. The volume of the neurons filling this area on a typical coverslip was estimated using 800 μm³ for the volume of a single cortical neuron soma and the average neuron density on a coverslip (from microscopic analysis). The concentration was then corrected for the difference between the volume of the cells and volume illuminated by the excitation beam in a cuvette. The calculated value was slightly less than the loading concentration of 5 μM (see Table 2).

Determination of cellular MT level. MT levels of cortical cultures were determined using the cadmium-hemoglobin affinity assay, essentially as described previously (14). Cadmium was determined by ICP-optical emission spectrometer (Varian) and protein by Bio-Rad method, as described above.

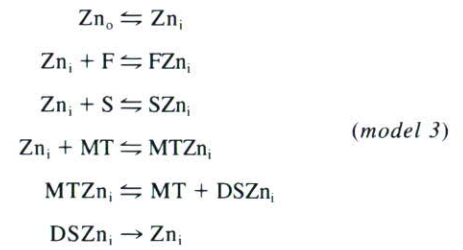
Modeling methods. Three models of Zn²⁺ homeostasis with increasing complexity were used in the analysis. The simplest model, the buffer model, contains only reactions describing Zn²⁺ transport, binding to fluorophore, and Zn²⁺ buffering:



where Zn_o is extracellular Zn²⁺; Zn_i is intracellular Zn²⁺; F and FZn_i are the concentrations of free and bound fluorophore, respectively; and S and SZn_i are the concentrations of free and bound buffer, respectively. The second model, the muffler model, adds reactions to the buffer model for Zn²⁺ “muffling” and sequestration into a “deep store” and Zn²⁺ leak from the deep store:



where DSZn_i is the concentration of Zn²⁺ in the deep store. In the third model, the MT as muffler model, it is assumed that MT is the part of the “muffler” that sequesters Zn²⁺ into the deep store, and reactant, S, is a simple buffer, as in model 1 above.



MT reactions for the seven Zn²⁺ binding sites are modeled in more detail as described below.

In the experiments, fluorophore fluorescence was monitored under a number of conditions, before or after exposure to increased extracellular Zn²⁺, including the addition of pyridoxine, EDTA, TPEN, and CQ, and the model was extended to incorporate these conditions when necessary, as described below. The chemical reactions were modeled with standard differential equations that were solved with Gepasi 3 (44), Copasi (29), and MATLAB (The MathWorks, Natick, MA). Rate constant and initial concentration values for the base models are collected in Tables 1 and 2.

Zn²⁺ transport. Zn²⁺ transport, represented above simply as Zn_o ⇌ Zn_i, was modeled with reversible Michaelis-Menten kinetics with V_{max} and K_m being the same for influx and efflux. The value for K_m was measured experimentally as reported below. V_{max} was fixed from the increase in total Zn²⁺ content measured experimentally after 30 min of exposure to 10 μM extracellular Zn²⁺. In most simulations, extracellular Zn²⁺ was 30 μM (or far larger than the intracellular concentration), and results were the same, whether or not we used standard or reversible Michaelis-Menten kinetics to describe transport because efflux was negligible. Efflux came into play only in the few simulations when EDTA was added to the bath, and in these cases precise parameter values for the reverse path were not critical.

Binding to fluorophore. Zn²⁺ binding to the fluorophore ZnAF-2F, represented in the model as Zn_i + F ⇌ FZn_i, is well characterized. The fluorophore has a K_d of 5.5 nM, and on and off binding rates at 25°C have been measured (28). Because our experiments were done at physiological temperature, we have increased these binding rate values, assuming a temperature coefficient (Q₁₀) value of 3. This proved necessary to match experimental results when EDTA was applied extracellularly.

Zn²⁺ muffling and leak from a deep store. Muffling is a term first used by Thomas et al. (58) to lump together the many additional

Table 1. Parameter values used in the models

Parameters	Reaction	Buffer Model (Model 1)	Muffler Model (Model 2)	MT as Muffler (Model 3) [MT] = 2.0, 1.0, 0.5, 0.15 μM
K _m , V _{max}	Zn _o ⇌ Zn _i	4.64, 0.26	4.64, 0.26	4.64, 0.26
k _{f1} , k _{t2}	F + Zn _i ⇌ FZn _i	11.84, 0.0651	11.84, 0.0651	11.84, 0.0651
k _{b1} , k _{b2}	S + Zn _i ⇌ SZn _i	10, 0.78	80, 0.0064	80, (0.008, 0.009, 0.015, 0.0175)
k _{d1} , k _{d2}	SZn _i ⇌ DSZn _i + S		0.03, 0.024	
k _l	DSZn _i → Zn _i		0.0062	0.0145
k _{m41} , k _{m42}	Zn _i + M4 ⇌ M4Zn _i			80, 1.28e ⁻⁴
k _{m51} , k _{m52}	Zn _i + M5 ⇌ M5Zn _i			80, 3.2e ⁻³
k _{m61} , k _{m62}	Zn _i + M6 ⇌ M6Zn _i			80, 8e ⁻³
k _{m71} , k _{m72}	Zn _i + M7 ⇌ M7Zn _i			80, 1.6
k _{r71} , k _{r72}	M7Zn _i ⇌ DSZn _i + M7			(3, 6, 12, 30), 3e ⁻⁵
k _{r61} , k _{r62}	M6Zn _i ⇌ DSZn _i + M6			(3, 6, 12, 30), 0.06
k _{r51} , k _{r52}	M5Zn _i ⇌ DSZn _i + M5			(3, 6, 12, 30), 0.15
k _{q1} , k _{q2}	2CQ _i + Zn _i ⇌ CQ ₂ Zn _i	50, 5	50, 5	50, 5
k _{CQ1} , k _{CQ2}	CQ _o ⇌ CQ _i , CQ ₂ Zn _o ⇌ CQ ₂ Zn _i	1.5, 1.5	1.5, 1.5	1.5, 1.5
k _{pyr}	Zn _o → Zn _i (pyridoxine)	0.052	0.052	0.052
k _{t1} , k _{t2}	T _i + Zn _i ⇌ T _i Zn _i	80, 2.064e ⁻⁸	80, 2.064e ⁻⁸	80, 2.064e ⁻⁸
k _{tp}	T _o ⇌ T _i , TZn _o ⇌ TZn _i	0.1, 0.1	0.1, 0.1	0.1, 0.1

Rates are in μM⁻¹·s⁻¹ or s⁻¹. Forward rate constant is given first in any pair. MT, metallothionein; CQ, clioquinol. See Table 2 for definitions of other acronyms.

Table 2. Initial resting concentrations used in the models

Reactant	Description	Buffer Model (Model 1)	Muffler Model (Model 2)	MT as Muffler (Model 3) [MT] = 2.0, 1.0, 0.5, 0.15 μM
Zn _o	Extracellular zinc	30	30	30
Zn _i	Intracellular zinc	1.047e ⁻³	1.047e ⁻³	1.047e ⁻³
F	Free fluorophore	3.9816	3.9816	3.9816
FZn _i	Zinc-bound fluorophore	0.7584	0.7584	0.7584
S	Free buffer (muffler)	1202.8	19	20.913, 30.885, 42.81, 51.303
SZn _i	Zinc-bound buffer	16.192	234.09	219.08, 231.11, 239.19, 245.69
DSZn _i	"Deep store" zinc		15.194	20.494, 13.666, 7.886, 3.333
M4	Free MT sites 1-4			1.22e ⁻² , 6.1e ⁻³ , 3.0e ⁻³ , 9.0e ⁻⁴
M4Zn _i	Zinc-bound MT sites 1-4			7.988, 3.994, 1.997, 0.5991
M5	Free MT site 5			0.9749, 0.738, 0.452, 0.147
M5Zn _i	Zinc-bound MT site 5			1.025, 0.262, 0.048, 0.003
M6	Free MT site 6			1.392, 0.869, 0.478, 0.149
M6Zn _i	Zinc-bound MT site 6			0.608, 0.131, 0.022, 0.001
M7	Free MT site 7			1.964, 0.989, 0.497, 0.1496
M7Zn _i	Zinc-bound MT site 7			0.036, 0.011, 0.003, 0.0004
CQ _o	Free extracellular CQ	0 or varies	0 or varies	0 or varies
CQ ₂ Zn _o	Bound extracellular CQ	0 or varies	0 or varies	0 or varies
CQ _i	Free intracellular CQ	0	0	0
CQ ₂ Zn _i	Bound intracellular CQ	0	0	0
T _o	Free extracellular TPEN	0 or 170	0 or 170	0 or 170
TZn _o	Bound extracellular TPEN	0 or 30	0 or 30	0 or 30
T _i	Free intracellular TPEN	0	0	0
TZn _i	Bound intracellular TPEN	0	0	0
Zn _{total}	Total resting zinc	17	250	250
Capacity	Steady state (Zn _o = 30 μM)	1.25 mM	1.5 mM	1.5 mM

Values are in μM. TPEN, *N,N,N',N'*-tetrakis(2-pyridylmethyl)ethylenediamine.

processes that act to reduce the change in ion concentration. The muffling process is the most difficult to represent in the model, precisely because the actual muffling processes are not known. Several approaches are possible that include one or more "buffer equivalents" (26) and/or one or more stores, and we have examined some of the possibilities here.

In *model 1*, the muffler is a simple buffer. In *model 2*, the muffler is a buffer that binds Zn²⁺, and this buffer also transfers Zn²⁺ to a deep store as given by the SZn_i ⇌ S + DSZn_i reaction. The deep store is an immobile unreactive pool of Zn²⁺ in the cell that may represent Zn²⁺ in mitochondria, the Golgi apparatus, other organelles, or various high-affinity metalloenzymes. Because the capacity of the deep store is finite, there must be a leak from the deep store, which we represent by DSZn_i → Zn_i. The capacity of the deep store was determined experimentally as noted below, and this constrained parameter value choices because, in most simulations, capacity is approximately $k_{d1}[S]_{total}/k_{t1}$, where $[S]_{total}$ is $[S] + [SZn_i]$ (where brackets denote concentration), and the constants are defined in Tables 1 and 2. In *model 3*, the muffler is composed of a buffer and MT. In this model, the buffer is a simple buffer, and it is MT alone that sequesters Zn²⁺ into the deep store. Deep-store Zn²⁺ capacity again provides constraints on parameter value choices; here it is the ratios of the MT sequestering rate constants, k_{t51} , k_{r61} , and k_{t71} , to the leak rate constant that are constrained by the deep-store Zn²⁺ capacity for a given MT concentration.

Binding to MT. MT can bind seven Zn²⁺ ions, with four sites binding more avidly than the other three. To represent this in the model, we consider different classes of binding sites and model the concentration of binding sites rather than MT concentration itself. In the model, the K_d for the first four binding sites was 1.6 pM. The K_d for the fifth, sixth, and seventh binding sites was 40 pM, 100 pM, and 20 nM, respectively (39). The individual on and off rate constants are not known, but were constrained by the experimental data. Typically, on rates were 80–100 × 10⁶ M⁻¹·s⁻¹ with off rates chosen according to the K_d value. MT concentration was 0.15, 0.5, 1, or 2 μM in the models, representing 1.05, 3.5, 7, or 14 μM of Zn²⁺ binding sites. In *model 3*, the three lowest affinity Zn²⁺ binding sites of MT could

transfer Zn²⁺ to and from the deep store, with sequestration efficiency dependent on the K_d of the binding site.

Pyridithione as an ionophore. Pyridithione is known to be a Zn²⁺-selective ionophore, and it was often applied experimentally after the cells were exposed to high levels of extracellular Zn²⁺ for a period of time. We have not found it necessary to model its action in a manner more complicated than a first-order term, where the increase in intracellular Zn²⁺ over time is represented by $k_{pyr}([Zn]_o - [Zn]_i)$, with the value of pyridithione rate constant k_{pyr} set to match the experimental data.

EDTA. In some experiments, 100 μM EDTA were added to remove extracellular Zn²⁺. EDTA can bind calcium and magnesium as well as Zn²⁺. Given K_d values for Zn²⁺, calcium and magnesium of 3.2 × 10⁻¹¹, 2 × 10⁻⁵, and 1.76 × 10⁻³ μM, respectively, and extracellular Zn²⁺, calcium, and magnesium concentrations of 30, 500, and 1,000 μM, respectively, we calculated that the addition of 100 μM EDTA would reduce $[Zn]_o$ to 0.3 nM (in loCa Locke's solution). In the model, we set $[Zn]_o$ to this value when EDTA was added in the experiment.

TPEN. TPEN is added to remove Zn²⁺ from the system. Unlike EDTA, TPEN will cross the cell membrane. In the model, we assume TPEN binding with Zn²⁺ in the extracellular space is at equilibrium, and, with its K_d for Zn²⁺ at 2.58 × 10⁻¹⁶ M, addition of 200 μM TPEN to the extracellular space will make extracellular Zn²⁺ = 4.55 × 10⁻¹⁷ M or essentially zero. When the experiment had 30 μM of extracellular Zn²⁺ before the addition of 200 μM TPEN, the model assumed that the concentrations of free and Zn²⁺-bound TPEN, $[T]_o$ and $[TZn]_o$, were fixed at 170 and 30 μM, respectively. When TPEN was added after EDTA, we did not model the competition between the two for Zn²⁺; results were virtually identical, whether $[T]_o$ and $[TZn]_o$ were 170 and 30 μM or 200 and 0 μM to start. Free and Zn²⁺-bound TPEN cross the membrane according to their concentration gradients with rate constant k_{tp} , which is constrained by the rate of fluorophore fluorescence decay seen in the experiments. We use 0.1 s⁻¹ for k_{tp} and 80 × 10⁶ M⁻¹·s⁻¹ and 2.06 × 10⁻⁸ s⁻¹ for the on and off rates for Zn²⁺ binding to intracellular TPEN, as

these values provide the rapid decay time course observed experimentally.

CQ. CQ is a Zn^{2+} chelator that uses two molecules to bind one Zn^{2+} ion (18). When CQ is added extracellularly, we assume that binding with Zn^{2+} is at equilibrium before CQ crosses the cell membrane, and that, because the extracellular space is large compared with the intracellular space, the extracellular concentrations remain constant during the course of the experiment. Consequently, the constant extracellular concentrations of free and Zn^{2+} -bound CQ, $[CQ]_o$ and $[CQ_2Zn]_o$, are:

$$[CQ]_o = \frac{K_{CQ}}{4[Zn]_o} \left(\sqrt{1 + \frac{8[Zn]_o[CQ]_o}{K_{CQ}}} - 1 \right) \quad (1)$$

$$[CQ_2Zn]_o = 0.5 ([CQ]_o - [CQ]_o)$$

where $[CQ]_o$ is the total concentration of CQ added to the extracellular media, and K_{CQ} is the dissociation constant set to 100 nM (18). Because CQ is lipophilic, it readily enters the membrane. We assume that free and Zn^{2+} -bound CQ cross the membrane, according to their concentration gradients, with a rate constant of 1.5 s^{-1} . We use $50 \text{ M}^{-1} \cdot \text{s}^{-1}$ and 5 s^{-1} for the on and off binding rate constants for Zn^{2+} binding to intracellular CQ. These values were chosen to fit the experimental data.

Statistical analysis. For image analysis, representative cells were selected, and cell bodies defined the limits of individual regions of interest. Average pixel intensity for all regions was averaged to obtain mean \pm SE. Where appropriate, data comparisons were analyzed by one-way ANOVA, followed by Tukey's multiple-comparison test. Differences in the means were judged significant when $P \leq 0.05$.

RESULTS

Experimental analysis of Zn^{2+} influx and increases in intracellular free Zn^{2+} in cultured neurons. Figure 1, A–D, shows representative images of cortical neurons exposed to various experimental conditions, and Fig. 1E shows the results of quantitative analysis of Fig. 1, A–D. Neurons loaded with ZnAF-2F in nominally zero extracellular Zn^{2+} (5-min exposure to 100 μM EDTA/loCa Locke's buffer; without Zn^{2+} addition) show a diffuse fluorescence in the cell body and nucleus with no evidence of compartmentalization (Fig. 1A). ZnAF-2F fluorescence appears also in cell processes, but this is not as readily apparent as cell body fluorescence in the images shown in Fig. 1. The same pattern of diffuse intracellular fluorescence is seen even after maximum Zn^{2+} uptake in the

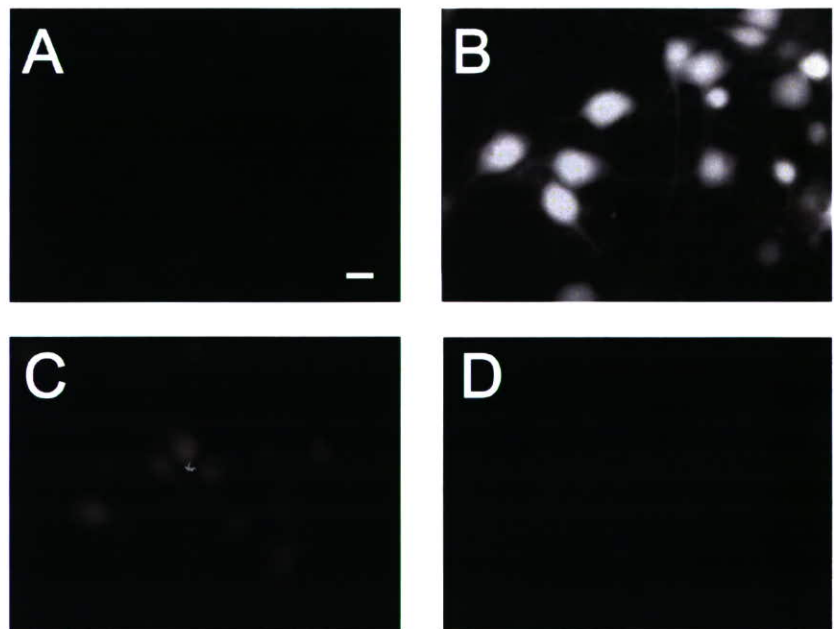
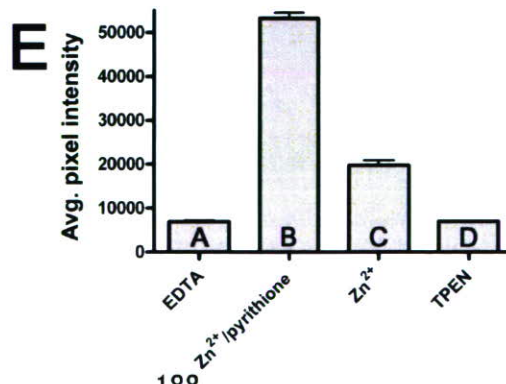


Fig. 1. Cortical neurons attached to glass coverslips were loaded with 5 μM ZnAF-2F, then placed in a cuvette containing low-calcium (loCa) Locke's buffer containing 100 μM EDTA (A), 30 μM Zn^{2+} plus 5 μM pyrithione (B), 30 μM Zn^{2+} (C), or same as in B, followed by 200 μM *N,N,N',N'*-tetrakis(2-pyridylmethyl)ethylenediamine (TPEN) for 5 min (D), then coverslips were moved to a perfusion chamber with the same buffer for live-cell imaging. Cell bodies were analyzed for average pixel intensity, and those data are shown in E. Each bar represents mean \pm SE ($n = 7$ individual cells on one coverslip as pictured in A–D). A Tukey multiple-comparison test (GraphPad Prism, version 4.03) showed that, for any column pair, $P < 0.001$, except for EDTA vs. TPEN, where $P > 0.05$. Size bar = 10 μm .



presence of 5 μM pyrithione/30 μM Zn²⁺ (Fig. 1B). In Fig. 1C, neurons were incubated with 30 μM Zn²⁺ only for 5 min, and an increase in intracellular fluorescence intensity was clearly visible as well. Finally, neurons treated with Zn²⁺ and pyrithione were subsequently treated with 200 μM TPEN, showing that the increase in intracellular fluorescence was completely reversed (Fig. 1D). These data verify the basic assumptions of the computational model of Zn²⁺ homeostasis; i.e., that intracellular ZnAF-2F and free Zn²⁺ are free to equilibrate, ZnAF-2F is not compartmentalized, ZnAF-2F does not show rapid photobleaching or leakage, and that newly entering Zn²⁺ is free to equilibrate with the resident pool of free Zn²⁺.

Determination of the total Zn²⁺ and MT in resting cortical neurons. The total cellular Zn²⁺ in resting cells was obtained from ICP-MS analysis of nitric acid digests of cultured neurons resuspended in chelex washed buffer (see Table 3). In addition, we determined the concentration of several metals in the NB media used for maintaining the neurons in culture (see Table 4). NB media had only trace amounts of Mn; Cu was approximately one-fourth the value of Zn²⁺ (Zn²⁺ \approx 1 μM), and Fe was the highest (\approx 8 μM). The total Zn²⁺ content of resting cortical neurons cultured in NB media (with B27 supplement, 0.5 mM glutamine) was 12.3 ± 0.6 nmol/mg cell protein (Table 3). Using straightforward estimates of pyramidal neuron soma volume (800 μm^3) and an estimate of the number of neurons per milligram protein (or the density of a neuron being 1 g/ml and containing 2% protein) allowed the calculation of an average intracellular concentration for Zn²⁺ of \sim 250 μM . This value is comparable to the value of 150 μM estimated for the whole brain by very different methods (57) or in HT-29 cells (38). It is generally accepted that nearly all of this Zn²⁺ is either protein bound or sequestered in organelles, such that the free cytosolic Zn²⁺ concentration is picomolar to nanomolar (38). Total MT concentration was found to be 109.6 ± 13.0 ng/mg cell protein (mean \pm SE; $n = 3$). This value is about twice that determined previously for MT-1 levels only in cultured cortical neurons by radioimmunoassay (27). Using the calculation as described above to estimate total Zn²⁺ concentration yields a total cellular MT concentration of 0.34 μM .

Analysis of changes in the neuronal Zn²⁺ content after Zn²⁺ influx was increased. To stimulate Zn²⁺ influx, we increased extracellular Zn²⁺ to micromolar concentrations. Under these conditions, in the absence of plasma membrane depolarization, Zn²⁺ transporters provide the primary routes of net cellular Zn²⁺ influx or efflux (7). In addition, we measured cellular Zn²⁺ content after addition of the Zn²⁺ ionophore pyrithione plus Zn²⁺. Two methods were used to quantify the total neuronal Zn²⁺ uptake when influx was increased: ICP-MS analysis

Table 4. Inductively coupled plasma-mass spectrometry analysis of selected metals present in cell media

	Mn	Fe	Cu	Zn
NB media, B-27 supplement, 0.5 mM glutamine	0.001 ± 0.001	8.31 ± 0.42	0.286 ± 0.020	1.07 ± 0.040

Values are means \pm SE in $\mu\text{mol/l}$; $n = 3$. Concentrations were obtained in media before addition to cells.

(Fig. 2A) and ⁶⁵Zn²⁺ uptake (Fig. 2B). Every attempt was made to make these determinations under identical experimental conditions (except for the inclusion of ⁶⁵Zn²⁺). When estimating the change in Zn²⁺ content using ICP-MS analysis, it was necessary to subtract the Zn²⁺ content measured in resting cells (see Table 3). Exposure of neurons to 10 μM extracellular Zn²⁺ for 30 min resulted in an increase in Zn²⁺ content of \sim 25 nmol/mg cell protein by ICP-MS analysis (estimates of ⁶⁵Zn²⁺ uptake were slightly lower, compare Fig. 2, A and B). However, it is important to consider if any portion of this increase in neuronal Zn²⁺ represented extracellular plasma membrane binding, as this would affect the parameter values used to constrain the model. Previous studies have shown significant extracellular binding when K562 erythroleukemia cells were exposed to micromolar extracellular Zn²⁺ (9). To estimate extracellular binding, cultured neurons were exposed to 10 μM ⁶⁵Zn²⁺ for 30 min, and then 100 μM EDTA was added. As shown in Fig. 2C, addition of 100 μM EDTA resulted in a rapid ⁶⁵Zn²⁺ release, amounting to \sim 40% of the observed increase in cellular Zn²⁺ content. This amount of Zn²⁺ was considered surface bound, because later experiments (see Fig. 6) showed that efflux was nominal over the same time period. Thus the Zn²⁺ content of neurons exposed to 10 μM Zn²⁺ for 30 min was estimated to be 570 μM . Zn²⁺ uptake when Zn²⁺ was added with pyrithione was increased nearly threefold over Zn²⁺ alone, as measured by ICP-MS analysis (Fig. 2A) and would be estimated to reach an average concentration of 1.5 mM. In addition, the ICP-MS analysis showed that the conditions of increased net Zn²⁺ uptake were quite specific for Zn²⁺. No observable change in the Mn, Fe, or Cu content could be detected under either of the conditions studied (data not shown).

A kinetic analysis of Zn²⁺ influx and corresponding changes in intracellular ZnAF-2F fluorescence in cortical neurons. Kinetic data were easily quantified by direct measurement (i.e., without image analysis) using a spectrofluorometer, which provided a continuous read out of fluorescence changes. Under resting conditions, it is presumed that neurons exist in a steady state with overall balanced Zn²⁺ influx and efflux. When "contaminating" Zn²⁺ is removed from the extracellular buffer, net influx should be reduced to zero. Thus, after elimination of Zn²⁺ influx by addition of 100 μM EDTA, ZnAF-2F fluorescence decreased slightly to a new steady state (Fig. 3A). The addition of pyrithione had no effect in the absence of extracellular Zn²⁺. The new steady state obtained was reduced further by the addition of TPEN. The level of intracellular free Zn²⁺ in the presence of TPEN is below the detection limit of ZnAF-2F; thus measured fluorescence after TPEN addition must represent autofluorescence and background light scattering (Fig. 3A). Thus, under resting conditions (i.e., time = 0),

Table 3. Inductively coupled plasma-mass spectrometry analysis of selected metals present in rat cortical neurons

	Mn	Fe	Cu	Zn
Cultured neurons	0.126 ± 0.01	8.05 ± 0.80	2.44 ± 0.07	12.3 ± 0.60

Values are means \pm SE in nmol metal/mg cell protein; $n = 4$. Protein was determined by the Bio-Rad assay. Cultured neurons were maintained in neurobasal (NB) media with B27 supplement and 0.5 mM glutamine added. Cells were washed in low-calcium Locke's buffer/100 μM EDTA before analysis.